Light harvesting hexamolybdenum cluster integrated with the 3D ordered semiconductor inverse opals for optoelectronic property

T.K.N. Nguyen, Fabien Grasset, S. Cordier, N. Dumait, S. Ishii, H. Fudouzi, T. Uchikoshi

Light harvesting hexamolybdenum cluster integrated with the 3D ordered semiconductor inverse opals for optoelectronic property

Thi Kim Ngan Nguyen[1], Fabien Grasset[2,3], Stéphane Cordier[3], Noée Dumait[3], Satoshi Ishii[4], Hiroshi Fudouzi[5], Tetsuo Uchikoshi[2,5]

[1]International Center for Young Scientists, Global Networking Division, National Institute for Materials Science, 1-2-1 Sengen, Tsukuba, Ibaraki 305-0044, Japan

[2]CNRS–Saint-Gobain–NIMS, IRL3629, Laboratory for Innovative Key Materials and Structures, National Institute for Materials Science, 1-1 Namiki, Tsukuba, Ibaraki 305-0044, Japan

[3]Univ. Rennes-CNRS-Institut des Sciences Chimiques de Rennes, UMR6226, 35000 Rennes, France

[4]Photonics Nano-Engineering Group, International Center for Materials Nanoarchitectonics, National Institute for Materials Science, 1-1 Namiki, Tsukuba, Ibaraki 305-0044, Japan

[5]Research Center for Functional Materials, National Institute for Materials Science, 1-2-1 Sengen, Tsukuba, Ibaraki 305-0044, Japan

Corresponding author: Thi Kim Ngan NGUYEN

Full postal address: International Center for Young Scientists, National Institute for Materials Science (NIMS), 1-2-1 Sengen, Tsukuba, Ibaraki 305-0047, Japan

E-Mail address: NGUYEN.Thikimngan@nims.go.jp

ABSTRACT

Solar energy-harvesting materials have significantly contributed to the development of energy-saving applications for several decades. We have mainly used a new concept composed of the electrophoretic deposition technique and photonic crystal structural engineering to understand the tunable light-absorption and electronic conduction properties. A hexamolybdenum cluster compound (denoted as the Mo_6 cluster) was

successfully functionalized on a tin pyrophosphate semiconductor integrated within an inverse opal photonic crystal. The size of the periodical pores, surface modification, and chemical composition of the infiltration material of the inverse opal film have been investigated to control the photonic bandgap in the visible range and the efficiency of the deposited Mo_6 cluster. The photoactive Mo_6 clusters act as a visible light harvester and generate an efficient photo-induced current upon light absorption that is enhanced by a slow photon effect occurring at the photonic stopband edges. The electron and proton are transferred in the inorganic-organic network via hydrogen bonds by a hopping mechanism to generate a rapid photoconductivity response during light irradiation. Specific attention focused on the role of humidity and temperature regarding the reproducibility of the experiments and the photosensitivity of the nanocomposite. The suitable tunable photo-induced conduction property in organic-inorganic materials opens a new opportunity for the applicability of cluster-based compounds in visible optoelectronic devices.

KEYWORDS: hexamolybdenum atom cluster, optical material, 3D inverse opal structure, optoelectronic, visible light harvesting, surface chemistry

1. INTRODUCTION

Considering the serious global warming problem, the discovery of a solar energy-converting material in the Vis-NIR domain for optoelectronic devices, such as photodetectors, light emission devices, sensors, and dye-sensitized solar cells, has occurred [1-5]. Among the nanoarchitecture nanomaterials, the $[M_6L^i_8L^a_6]^{n-}$ cluster unit, composed of a central Mo_6 cluster, eight inner ligands at the face-capping position (L^i = halogen or chalcogen; i for inner), and six apical ligands at the terminal positions (L^a = halogen, OH^-, H_2O, N_3, $OCOC_nH_{2n+1}$, etc; a for apical.), has become attractive due to the delocalization of the valence electrons on the metal centers for producing interesting photochemical and redox properties [6-7]. These metal atom clusters (MCs) exhibit luminescence properties combined with high-quantum yields, a large Stoke shift for preventing absorption loss, strong absorption in the ultraviolet (UV)-Vis domain, photostability at room temperature, and facile processing. These advanced properties have been utilized in the design of optical-related devices, phosphorescent nanocluster

emitters, saving-energy devices, photodetectors, photoelectrodes for DSSC, and photocatalytic electrodes for water splitting [8-14]. In addition, the tunable photo-induced electronic property of the MC with functional semiconductors has been recently investigated which will be a fascinating property for optoelectronic devices [15-17]. Renaud et al. explored the potential of Mo_6 clusters as new nontoxic and stable inorganic sensitizers with amphoteric properties for light-emitting photoelectrodes that were achieved and integrated into solar cell devices [13]. The influence of light on the electrical properties of ionic conductors, the so-called opto-ionic property, around room temperature has become a hot topic, especially ionic conduction, which is crucial and very promising. A UV-Vis photodetector based on Mo_6 clusters embedded in a protonic conducting 2D material was demonstrated by Nguyen et al. It revealed that the reproducibility and stabilization of the ionic photocurrent response were verified upon light excitation at 540 nm which linearly depends on the relative humidity and temperature [12]. However, potential applications based on the cluster face many challenges due to the difficult control of a mono-dispersed cluster distribution, thermal and chemical stability, and production on a large scale. The combination of the nano-sized atom cluster with functional supporting materials; i.e., semiconductor, polymer, or hybrid, becomes an interesting solution in order to enhance the atom cluster's weakness. However, the charge transport between the cluster and the semiconductor is an important point to develop tunable photo-induced conducting properties.

Recently, the enhancement of the efficient photoconductivity response has been studied for visible light-harvesting materials, such as cadmium zinc telluride (CZT), cobalt-doped zinc ferrite oxide, or the use of specialized techniques, such as scalable photonic platforms based on silicon, and the band engineering of the TiO_2/Si heterojunction [18-21]. As is known, artificial photonic crystal inverse opal (IO) structures can propagate the angle-dependent refractive light by using the periodic variation in the dielectric contrast or reflective index contrast within a crystal [22-23]. Light scattered or/and diffracted from the different surfaces will produce a full or partial photonic bandgap (PBG). This PBG and its manipulation ability could be deeply understood in researching different infiltration material precursors, various synthesis routes, and structural depending applications. The interesting advantages of this structure are subsequent inhibition of the

spontaneous emission, and the possibility to localize and enhance the emission or reflection of light. Moreover, in the 3D inverse opal photonic crystal, slow photon-induced light absorption is considered more than the photonic bandgap-induced light reflection for enhancing the generation of an electron-hole pair upon illumination [24]. The 3D-ordered porous structure has been potentially developed for photodetectors, photoelectrodes for water splittings, photocatalysts, oxygen or hydrogen evolution reactions, and light-trapping parts for dye-sensitive solar cells [25-31]. In addition, the ordered porous inverse opal supplies a large area for the active site, a promising loading possibility of the active materials, necessary transmittance for the transparent conducting substrate, controllable photon absorption, etc. [29, 30]. The first goal of this study is to use the inverse opal photonic crystal to enhance the visible light absorption of the Mo_6 cluster.

The metal atom cluster exhibits an excellent photoactive property upon UV-Vis light illumination to generate electron-hole pairs, however, the excited electron will immediately recombine with the hole without transporting in the network. The second goal of this study is to select metal oxide semiconductors exhibiting high electron and ionic conductivities as a carrier for producing a high photoconductivity response. As is known, proton metallic phosphate conductors (MP_2O_7; M = Sn, Al, Mg, In, etc.) are potential candidates which have been studied in electrochemical device, such as intermediate-temperature proton conductors for fuel cells, batteries, gas sensors, NIR phosphor-converted light-emitting diode, etc. [32-38]. The protonic and electron-hole conductivity of SnP_2O_7 essentially occurs in the bulk material rather than on the surface and is influenced by the structural characteristic, single cubic crystal or amorphous one [39, 40].

Until now, only one idea based on a silica opal photonic crystal and atom metal cluster has been reported with an increase in the emission intensity in the energy range of the passband [41]. For the first time, the SnP_2O_7 proton conductor integrated with an inverse opal photonic crystal functionalized with the photoactive Mo_6 cluster iodide ($[\{Mo_6I^i_8\}I^a_4[H_2O]^a_2].y\ H_2O$) was successfully fabricated by using electrophoretic deposition (EPD), a short-time consuming and efficient technique. The Mo_6 iodide cluster

compound, $Cs_2[\{Mo_6I^i_8\}I^a_6]$ (noted CMI), was selected as the cluster precursor due to its strong absorption in the visible light range and photostability under long irradiation [42]. The hydrophilic surface modification of the SnP_2O_7 inverse opal film by using citric acid also enhanced the loading concentration of the Mo_6 cluster. The enhancement of the visible light absorption of the Mo_6 cluster was obtained which is a result of the slow photon effect at the PBG edges due to the inverse opal structure. The optimizations of the pore size and ordered porous structure could control the PBG position in order to enhance the photonic energy absorption in the desired wavelength region. The photo-induced current phenomenon was investigated by the photoconductive response generated by AC and DC electric field generators upon light irradiation. The photoconductivity response upon the visible light irradiation from 400 to 580 nm is linearly dependent on temperature and humidity. This concept provided many interesting characteristics which are relevant for designing environmental sensors, a photodiode for a solar cell, or a photodetector.

2. EXPERIMENTAL

2.1 Preparation of SnP_2O_7 IO films and citric acid-modified SnP_2O_7 IO films

Figure 1 shows a schematic diagram of the simple methods to prepare the SnP_2O_7 IO films. Aqueous solutions containing 8 wt% of monodispersed polystyrene (PS) beads were prepared by the standard emulsion polymerization method [43]. The average sizes (240, 288, and 308 nm) of the PS beads were measured from a scanning electron microscope image. The anodic EPD was used to fabricate the PS-based photonic crystal film with the periodic arranged face-centered cubic lattice. The simple EPD system included two electrodes; i.e., indium tin oxide-coated glass (ITO) (Geomatec Co., Ltd., Tokyo, Japan; 6.15-7.27 Ohm/sq) with a surface area of 2×3 cm^2 treated in ethanol and stainless steel with a surface area of 2×3 cm^2 treated in ethanol. The distance between the electrodes was fixed at 0.5 cm. The electrodes were connected to a Source Meter (Keithley Model 2400, Ohio, USA) as an electric field generator. The aqueous 8wt% PS solution was diluted by ethanol (99.5%, Nacalai Tesque Co., Ltd.) at the volume ratio of 15/85 which is an optimized ratio to obtain a good periodic structure [44]. The EPD opal films were optimally prepared at 10 or 12 V for 1 minute.

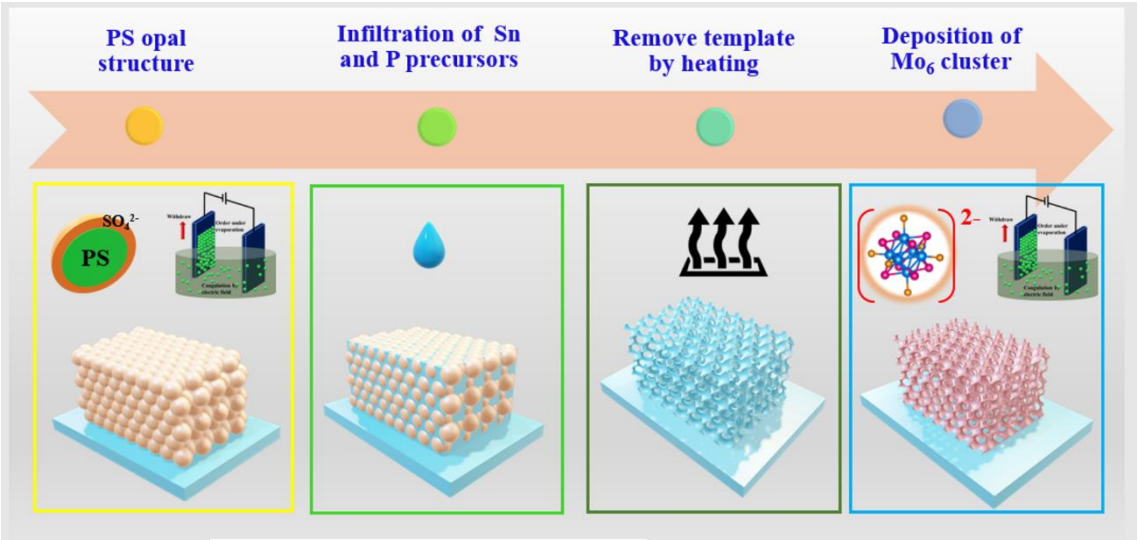

Figure 1. Schematic diagram of the fabrication process of Mo_6 cluster-deposited SnP_2O_7 IO nanostructure using a PS-bead template and electrophoretic deposition (EPD).

The precursor solutions for the infiltration process were prepared by dissolving tin tetrachloride ($SnCl_4 \cdot 5H_2O$, 98%, Nacalai Tesque Co., Ltd.) into ethanol: H_2O (volume ratio of 10:1) at the concentration of 10%. The molar ratio between P (0.5 ml) from phosphoric acid (H_3PO_4, 85%, Nacalai Tesque Co., Ltd.) and Sn precursors (1 g) was 2.6. The mixture was stirred for 3h under ambient conditions. Five drops of the solution mixture were then infiltrated into the PS-based photonic crystal film with an area of 5 cm^2, then slowly dried for 24 h. The SnP_2O_7 IO film was then fabricated by a thermal treatment program including 2 steps; i.e., fast heating to temperature T1 (500, 550, or 600°C) and slow heating from temperature T1 to temperature T2 (550, 600, or 650°C) for reducing cracking because of complete decomposition of the PS. The performance of SnP_2O_7 is illustrated following reaction **(1)** at high temperatures.

$$SnCl_4 + 2H_3PO_4 \rightarrow SnP_2O_7 + H_2O + 4HCl \quad (1)$$

The porous SnP_2O_7 IO film was then immersed in citric acid (98%, FUJIFILM Wako Pure Chemical Corporation) with a concentration of 52 mM for 10 minutes at 90°C, then heated at 100°C for 24 h in air. The acid-modified SnP_2O_7 IO film was stored at 50°C in air for the next fabrication process.

2.2 Preparation of the Mo_6 cluster-deposited SnP_2O_7 IO films

The hexamolybdenum cluster compound $Cs_2[\{Mo_6I^i_8\}I^a_6]$ was synthesized by the reaction of CsI (Alfa Aesar 99.9 %) and MoI_2 at a high temperature (700°C) following the procedure reported in a previous study [6]. The CMI powder was dissolved in acetone at the concentration of 1g/L by ultrasonication for 1h, then magnetic stirring for 72 h. The use of EPD to deposit the Mo_6 cluster in the porous SnP_2O_7 IO films was optimally studied at a voltage of 15 V and a deposition time of 2 minutes with a deposition area of 5 cm^2. The obtained films were dried at 100°C for 24 h to eliminate the residual solvent before the characterization and photocurrent response measurements. An abbreviated representation of the sample is SnPO IO_xca-MI, where 'SnPO' is SnP_2O_7, 'x' is the PS bead size (240, 288, 308 nm), 'ca' is citric acid, and the 'MI' is the hexamolybdenum iodine cluster.

2.3 Measurement of photocurrent response

A cell containing ITO glass coated by SnPO-IO_x, SnPO-IO_xca, SnPO-IO_xca-MI films (x = 240, 288, and 308 nm, the average size of PS bead) and a blank ITO glass with a measured area of 1.2×2 cm^2 connected to a micrometer. The film thickness was measured by a scanning electron microscope. The different UV-Vis light illuminations were generated by a 300 W compact Xenon light source (MAX-303, Asahi Spectra Co., Ltd.). A monochromator combined with an optical filter (transmittance ~ 80 %) was used to generate monochromatic light with a bandwidth of 10 nm, centered respectively on 350, 370, 410, 440, 540, and 580 nm. The real intensity of the photon energy arriving at the surface of the material film corresponded to almost 80% in the UV-Vis light range (350 nm – 600 nm) as revealed by the manufacturer. A source meter (VSP300, Potentiostat, BioLogic) was used to measure the DC photocurrent response of the films at a bias of 0.5 V with active area of 2.4 cm^2. The AC conductivity of the films was measured by a 1260A impedance analyzer (Solartron analytical, AMETEK Scientific Instruments) at a bias of 500 mV in the frequency range between 10^1 Hz and 10^7 Hz. All measurements were performed under controlled environmental conditions. The electrical conductivity was expressed by the following **Eq. 1**:

$$\sigma = l/(R.A) \quad (1)$$

where σ is the electrical conductivity, l is the thickness of the film, A is the area of the sample (1×1 cm^2), and R is the total resistance measured by Electrochemical Impedance Spectroscopy (EIS).

2.4 Characterization

The morphology characteristics were analyzed by field emission scanning electron microscopy (FE-SEM, SU8000, Hitachi High-Technologies Corp.) at 10 kV coupled with an energy-dispersive X-ray (EDX) analysis device. High-resolution (HR) observations of the powder were performed by an HR-transmission electron microscope (HR-TEM) (JEOL JEM 2100F) equipped with an EDX analysis device. The X-ray powder diffraction (XRD) patterns were recorded at room temperature at the 2-theta angle in the range of 10° and 60° using a SmartLab diffractometer (RIGAKU, 40 kV and 30 mA) with Cu Kα radiation (λ = 1.54 Å), a step size of 0.02° and a scan speed of 1°/min. Le Bail fittings were performed using the FullProf program included in the WinPLOTR software [44, 45]. The zero-point shift, asymmetry parameters, lattice parameters, and β angle were systematically refined, and the background contribution was manually estimated (**Tab. SI1**). The typical chemical vibration of the powder was recorded by Fourier transform infrared spectroscopy (FTIR) (Thermo Scientific Nicolet 4700) in the wavenumber range from 4000 to 400 cm^{-1} using a KBr pellet. The transmittance spectra of the IO films were measured by UV-Vis-NIR spectroscopy (V570, Jasco Corp.) in the wavelength range of 200 to 2000 nm at the scan rate of 400 nm/min. The specular reflectance spectra of the films were measured at the incidence angle of 5 degrees in the wavelength range of 200 to 2000 nm by using a UV-Vis-NIR spectrophotometer (Solidspec-3700, Shimadzu Corp.). The luminescent emitting spectra of the films were measured by high-performance fluorescence spectroscopy (JASCO FP8500) connected to a Xenon lamp at the scan rate of 500 nm/min. The electron binding energy spectra were measured by X-ray photoelectron spectroscopy (XPS) (PHI Quantera SXM (ULVAC-PHI)) using Al Kα radiation at 20 kV and 5 mA and taken-off angle of 45°. All the binding energies were calibrated concerning the C 1s peak of the adventitious carbon at 285 eV.

3. RESULTS AND DISCUSSION

3.1 Characterization of SnP_2O_7 IO film

Recently, the growth of photonic crystals by colloidal assembly routes has been particularly done but their potential in real-world applications still faces many challenges. The difficulties in controlling the external forces of suspension, solvent evaporation rate, withdrawal rate, and template concentration inhibited obtaining the chemical and thermal stability and well-ordered 3D porous structure [22]. EPD is a good technique that shows the flexibility of the substrate sizes and templates, short-time consumption, and uniform structure in comparison to the conventional methods [46]. FE-SEM images from **Fig. 2a** show the surface characteristic of the crystal opal films that were successfully fabricated using the anodic EPD at 10 V for 1 minute. The PS beads with the average sizes of 240 nm, 288 nm, and 308 nm were arranged to form well-ordered hexagonally packed photonic crystals that result in reflectance of green, red, and slight red colors as seen in the next photographs. The cross-section images of the films also showed good organization in a face-centered cubic (fcc) structure. The thickness of the different-sized opal films was recorded in the range of 5 to 10 μm (**Fig. SI1**) depending on the PS bead size with similar EPD parameters. The optical and photonic bandgaps were based on the UV-Vis transmittance spectra. The transmittance spectra from **Fig. 2b** show specific peaks centered at wavelengths of 563, 677, and 732 nm which indicated the partial photonic band gaps (PBGs) of the opal films corresponding to the 240, 288, and 308 nm-sized PS-bead templates, respectively. The PS spheres are well known without absorption in the blue/violet range. It means that the transmittance at 0 in this range comes from the scattering by the polystyrene spheres. For a larger PS bead size, the scattering appears stronger.

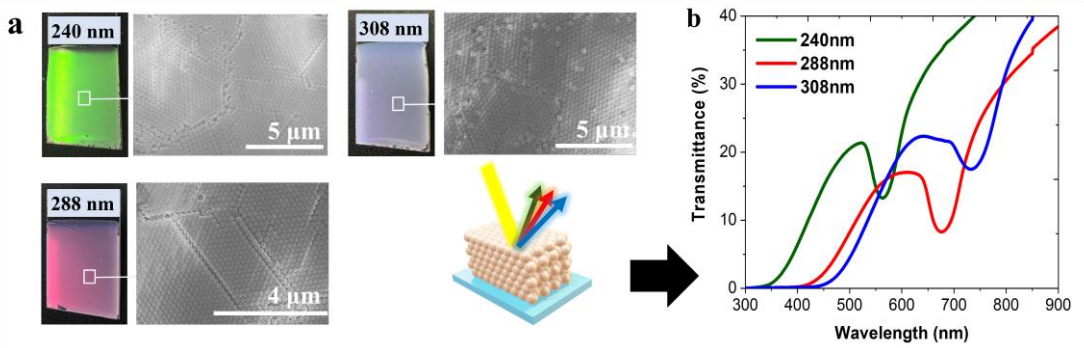

Figure 2. (a) Photographs of observed color and FE-SEM images of the opal films prepared by EPD (10 V, 1 minute) using different PS-bead sizes. (b) UV-Vis transmittance spectra and schematic image of the opal films.

For the first time, the SnP_2O_7 inverse opal structure was directly prepared by using the tin chloride precursor and phosphoric acid with the initial P: Sn molar ratio of 2.6. In this study, an annealing critical temperature of 600°C was effective to produce the cubic SnP_2O_7 structure and ordered porous inverse opal structure for the PBGs. The major reflections in the XRD pattern of the referenced SnP_2O_7 powder synthesized under the same conditions can be observed at specific 2-theta angles centered at 19.4° (111), 22.4° (200), 31.8 ° (200), 37.6° (311), 50.1° (331), 51.5° (420), and 56.8° (422) **(Fig. SI2)**. A Le Bail refinement of the whole samples has been performed and reasonably reliable factors have been obtained to confirm a space group of cubic *P a*-3 (a = b = c, $\beta \approx 90°$) (**Tab. SI1**). A similar pattern was verified for the SnP_2O_7 inverse opal film (SnPO-IO_{288}) with a weak intensity of crystallinity because of the porous structure (**Fig. 3a**). SnP_2O_7 has a cubic structure that shows corner-sharing SnO_6 octahedra and PO_4 tetrahedra containing the oxygen lattice ion on the surface as seen in **Fig. 3b** [47]**.** The FT-IR spectrum provides evidence for the symmetric and asymmetric stretching vibrations of the P-O bonds of the PO_4 groups at the wavenumbers of 1120 cm^{-1} and 960 cm^{-1} (**Fig. 3b**). The vibration band assigned to the Sn-O bonds was recorded at 498 cm^{-1}. This characteristic peak is in agreement with previous reports [48].

The UV-Vis transmittance spectra from **Fig. 3c** and **Fig. SI3** show the optical and PBGs of the SnPO-IO_x (x= 240, 288, 308) films annealed at different temperatures and ethanol/H_2O volume ratios fixed at 10/1. The SnP_2O_7 powder almost shows a low

transmittance under 300 nm due to its absorbance in this range. The initial molar ratio of P: Sn is more than 2 and the heat-treating temperature is higher than 500^{o}C which should be applied to definitely obtain the single cubic phase structure of SnP_2O_7 [49]. By the thermal treatment up to 550^{o}C, the SnP_2O_7 phase is performed and the IO film starts to form PBGs but their width is broad and asymmetric (**Fig. SI3)**. This can be a reason for the impurity of the SnO_2 phase which is not completely transferred to SnP_2O_7 [49]. As is known, the existence of the SnO_2 impurity with a high refractive index can expand the width of the stopband peak. However, at treatment temperatures up to 600^{o}C, the SnP_2O_7 IO films definitely show symmetrical PBGs at the wavelengths of 379, 457, and 502 nm, respectively, originating from the 240, 288, and 308 nm-sized PS beads (**Fig. 3c**). Although the single cubic phase structure of SnP_2O_7 was definitely created at 650^{o}C, the high-heating temperature can create much cracking and then destroy the ordered macropore structure. The low transmittance around the stopband positions in **Fig. 3c** (upper) possibly comes from the reflection, scattering, and refraction of the light caused by the inverse opal film. In order to clearly identify these inverse opal PBGs originating from the contribution of reflective light, the spectacular reflectance spectra were obtained at an incident angle of 5 degrees that show similar stopband peaks with a reflective light percentage lower than 15% (**Fig. 3c** under**)**.

From **Fig. 3d,** these photographs of the SnPO-IO_x (x= 240, 288, 308) films having pore sizes of about 223, 267, and 294 nm, respectively, are in agreement with the reflectance of the visual violet (379 nm), blue (457 nm), and cyan (502 nm) color (**Fig. 3c under)**. The obtained pore size was reduced from 5 to 7 % compared to the initial size of the PS bead as seen in the FE-SEM image. It can be influenced by the shrinkage of PS during the thermal treatment before the SnP_2O_7 crystal was formed. In addition, the low shrinkage also indicated a high SnP_2O_7 condensate. On the other hand, the thickness of the IO film was reduced by less than 10% from 5 to 10 μm while retaining the periodic structure (**Fig. 3d**). The role of water in this step contributes to the association of the Sn precursor that supports their transport in the voids between the PS beads. The pore size and inverse opal structure were confirmed in the STEM images (**Figs. 3e**). The elemental composition of tin pyrophosphate was confirmed to contain O, Sn, and P from the STEM-EDX mapping (**Fig. 3f**). By using the EPD technique, a SnP_2O_7 inverse opal photonic

crystal film showing the typical PBG was efficiently prepared in a short time, with a flexible thickness and active area on the TCO substrate. The thermal treatments at temperature T1 of 550^{o}C and temperature T2 of 600^{o}C with different heating rates were fixed to efficiently fabricate the SnPO-IO_x (x = 240, 288, 308) films for the next steps.

The approximate stopband position of the inverse opal can be calculated by a modification of Bragg's law taking into account Snell's law of refraction that is expressed in **Eq. 2** [50]:

$$\lambda_{max} = 2D\sqrt{\frac{2}{3}}\ \sqrt{f{n_1}^2 + (1-f){n_2}^2 - sin^2\theta} \quad (2)$$

Where, λ is the stopband position for the first-order Bragg diffraction, D is the PS bead size of the PhCs or pore size of IO, n_1 = 1 for air and n_2 = 1.59 for PS or n_1 = 1 for air and n_2 ~ 1.65 for SnP_2O_7 are the refractive indices, and θ is the incidence angle of the light which is 5^{o} in this measurement. Depending on the face-centered cubic (fcc) structure of the photonic crystals, the volume percentage (f) of the air and PS is 0.26 and 0.76, respectively. Based on **Eq.2**, the PS bead sizes of 240, 288, and 308 nm sizes confirmed by the FE-SEM images were used to calculate the PBGs which result in the wavelengths of 571, 685, and 732 nm, respectively. However, the experimental PBGs resulted in a small difference which was taken at 563, 677, and 732 nm as seen in **Table SI2**. The volume fraction of air was calculated from the measured data as more than 0.26 which is taken at the average fraction of 0.36 ± 0.02. The performance of the well-organized face-centered cubic structure is not completely preferred for a small PS bead size. In the case of the inverse opal structure, refractive indices of 1.65 for SnP_2O_7, the measured pore diameters (223, 267, and 294 nm), and stopband positions (379, 457 and 502 nm) were used to calculate the volume fraction of SnP_2O_7 based on **Eq. 2** (**Table SI2)**. It can be seen that the filling factors (f) of air in the SnP_2O_7 inverse opals almost reached more than 94%. As the result, the solid filling fractions of the inverse opal skeleton are 5, 6, and 6 % for the SnPO-IO_x (x= 240, 288, 308) films, respectively. In order to achieve a perfect inverse opal structure with a filling fraction close to 26% corresponding to a perfect fcc

structure, the filling quantity of the precursor solution, infiltration operation, and heating rate of the annealing should be appropriate.

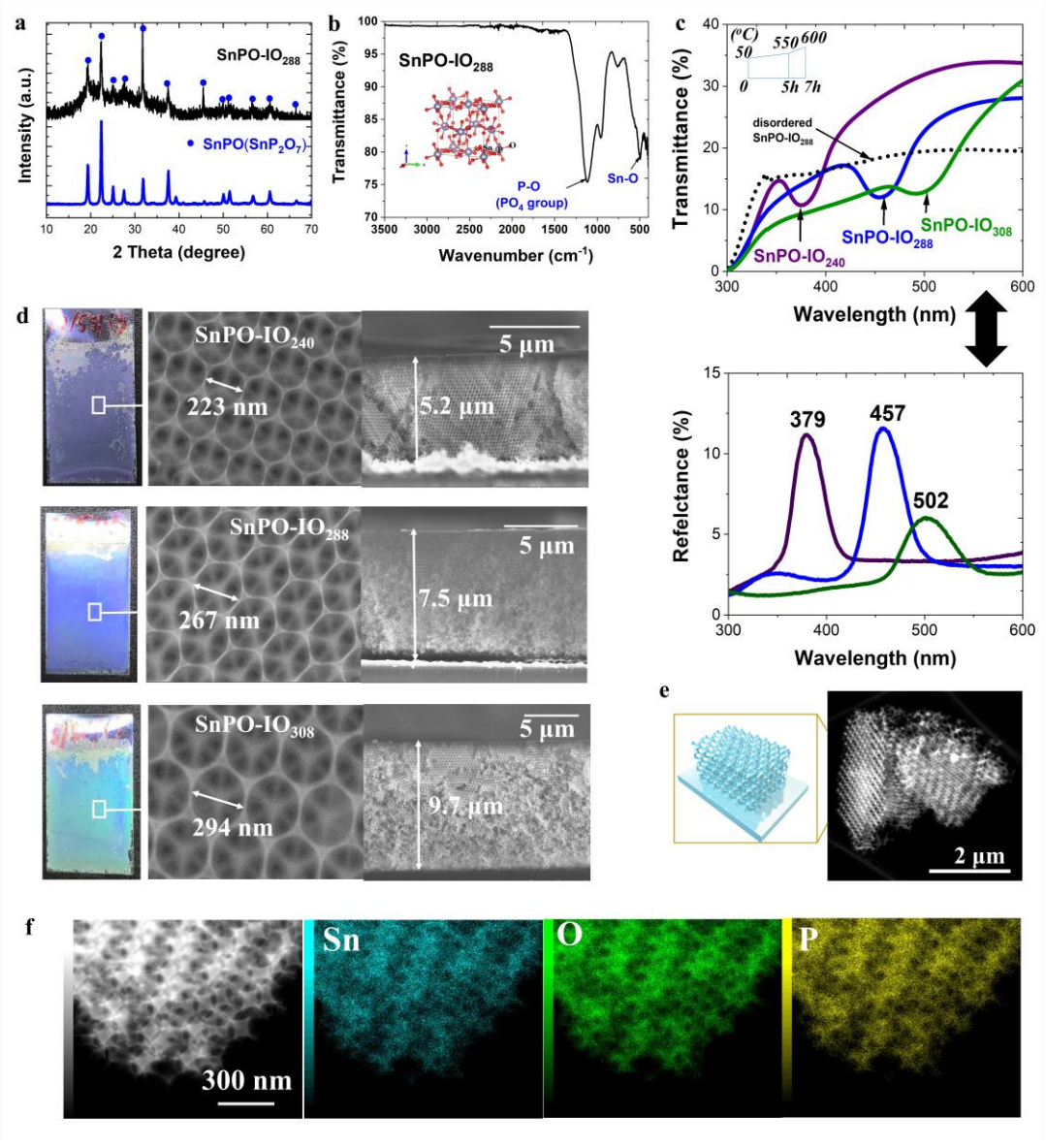

Figure 3. (a) X-ray diffraction diagrams of synthesized SnP_2O_7 powder and SnPO IO_{288} film, (b) Schematic illustration of the cubic SnP_2O_7 unit, and the FT-IR spectrum of SnPO-IO_{288}. (c) UV-Vis transmittance spectra and the specular reflectance spectra at the 5 degree incident angle of the SnPO-IO_x films (x= 240, 288, 308) with thermal treatment at T1 = 550°C and T2 =600°C. (d) Visual photographs and FE-SEM images (left) and cross-section SEM images of the SnPO-IO_x (x= 240, 288, 308) films (right). (e) HR-

TEM, (h) STEM and schematic image, and (f) STEM-EDX mapping of the SnPO-IO_{288} films.

3.2 Characteristics and optical properties of Mo_6 cluster-deposited SnP_2O_7 IO films

The CMI presents the efficiency of the visible light absorbing characteristics, which could be functionalized with an ionic conducting layer of a double hydroxide for tuning the photoconductivity response [12]. The obtained result showed a good photoconductivity response; however, the photosensitivity and photostability needed to be improved. The elimination of the apical iodide ligands of the Mo_6 cluster during the fabrication was also a reason for a reduction of the visible light absorption efficiency. In this study, the anhydrous proton conductor of tin pyrophosphate (SnP_2O_7) was chosen to be combined with the $[Mo_6I_{14}]^{2-}$ cluster unit precursor. As is known, the $Cs_2[\{Mo_6I^i_8\}I^a_6]$ solid-state compound is fully dissociated to form the Cs^{2+} cation and $[\{Mo_6I^i_8\}I^a_6]^{2-}$ cluster anion in solution. During EPD, hydronium and hydroxide ions, which were generated by the hydrolysis reaction of water in the dispersing medium, will replace some apical ligands to form the $[\{Mo_6I^i_8\}I^a_{6-x}\,[OH]^a_x]^{2-}$ ($0 \le x \le 6$) cluster anion in solution which possibly works in the EPD. However, **Fig. 4a** shows a photograph of the SnPO-IO_{288} deposited MI without modification by citric acid with the poor deposition of MI by using the EPD at 15 V for 2 minutes. Surface functionalization of the SnPO-IO_x (x = 240, 288, 308) films was then performed with two treatment steps in a citric acid solution at 90°C for 10 minutes and in air at 100°C for 24 hours (**Fig. 4b**). The dried SnP_2O_7 containing negatively-charged oxygen lattice ions can cause an opposite electrostatic interaction with the $[\{Mo_6I^i_8\}I^a_{6-x}\,[OH]^a_x]^{2-}$ ($0 \le x \le 6$) cluster anion. For this reason, the citric acid involving three carboxylic acid groups will generate the acidic surface and then becomes a bridge in order to make a second electrostatic interaction with the $[\{Mo_6I^i_8\}I^a_{6-x}\,[OH]^a_x]^{2-}$ ($0 \le x \le 6$) cluster anion. These bridges will create hydrogen bonds that are efficient to immobile MI on SnP_2O_7. Moreover, the functionalization by acid groups can improve the interface charge collection efficiency, which is important to carry the electron or ion transport in optoelectronic devices [51]. The deposition of MI on the SnPO-IO_{288} film was significantly improved as seen in the photograph with a homogeneous red color which was assigned to the MI nanocluster (**Fig. 4c).** Small cluster aggregates were also

observed on the surface of the SnPO-IO_{288}ca film. TEM and STEM were then used to confirm the distribution of MI that exists inside the pores of SnPO-IO_{288}ca-MI (**Fig. 4d, e**). STEM-EDX mapping indicated the composition elements of Sn, Mo, and I that confirmed MI nanoparticles with sizes less than 30 nm existing inside the pores (**Fig. 4f)**. **Fig. SI4** presents the element composition spectrum of Sn, I, and Mo with a poor observation of Cs. As is known, MI is synthesized at high temperatures with a crystal shape. The size of the aggregates of MI was confirmed in the range between 15 and 30 nm by the SEM image (**Fig. SI5**) which can deposit in the pore size of 267 nm from the SnPO-IO_{288}ca. The concentration and incomplete dissolution of MI in a solvent medium can create small nanoparticles composed of many 2 nm-sized MI clusters with the charge on the surface coming from the MI cluster unit. Only EPD can deposit the $[OH]^{a}_{x}]^{2-}$ ($0 \leq x \leq 6$) cluster anion without a counter cation which is an essential part of light harvesting.

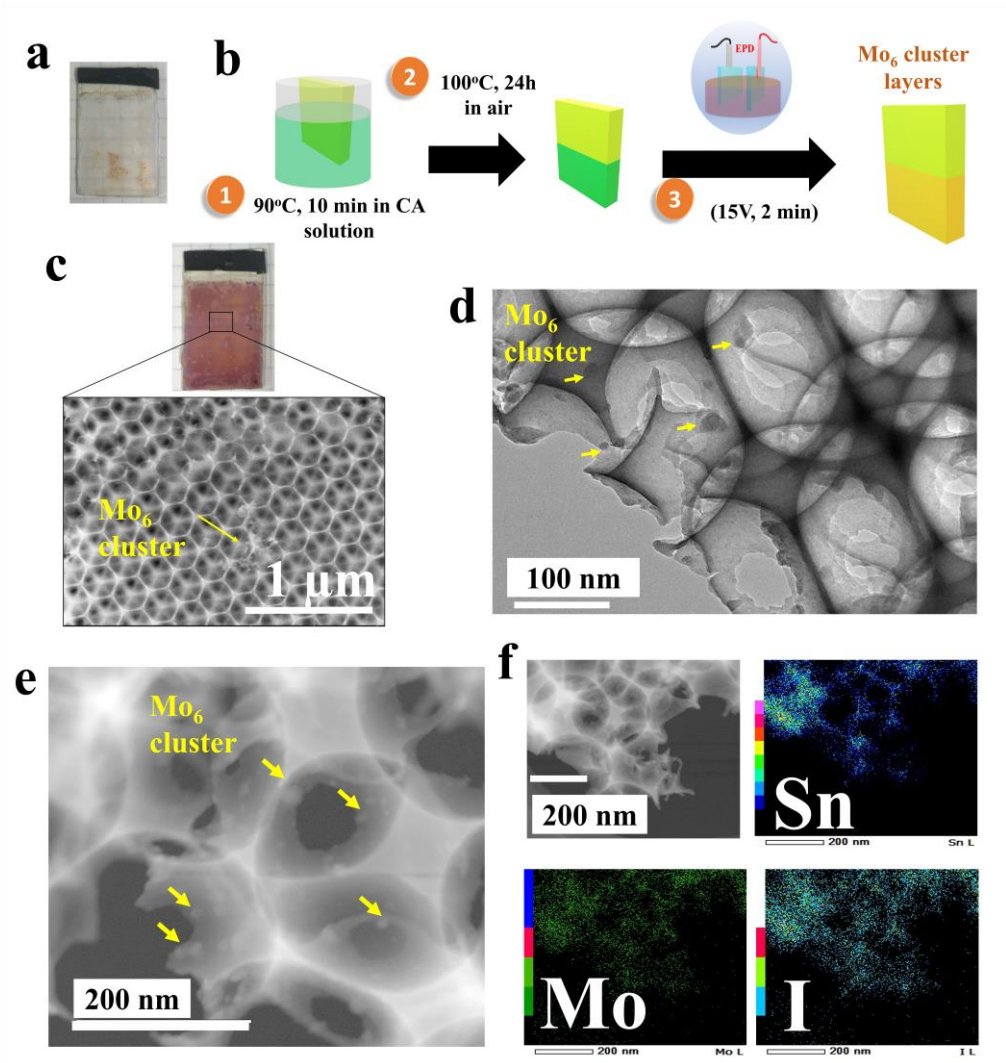

383

384 Figure 4. a) Photograph image of SnPO-IO_{288}-MI without citric acid modification. b)
385 Schematic diagram of the fabrication process photos of SnPO-IO_xca and SnPO-IO_xca-MI
386 films (x = 240, 288, 308). c) Photograph images and FE-SEM images of SnPO-IO_{288}ca-
387 MI with citric acid modification. (d) TEM, (e) STEM, and (f) STEM-EDX mapping
388 images of SnPO-IO_{288}ca-MI.

389

390 **Fig. SI6** summarizes the XPS spectra of SnPO-IO_{288} and SnPO-IO_{288}ca-MI. The binding
391 energy spectra of the Sn3d, P2p, C1s, O1s, Mo 3d, and I 3d regions were measured as
392 seen in **Table. SI3**. All binding energies were calibrated concerning the C1s peak of the
393 adventitious carbon at 285 eV. **Table 1** shows the atomic percentages of the elements of

SnPO-IO_{288} and SnPO-IO_{288}ca-MI. The atomic ratio of P and Sn is about 1.77. This ratio is almost unchanged after the EPD (~ 1.73) which indicates the chemical stability of the SnP_2O_7 inorganic IO film during the hydrolysis reaction. In the SnPO-IO_{288}ca-MI film, the concentration of carbon atoms increased 2.5 times due to the introduction of citric acid in comparison to SnPO-IO_{288} without acid treatment. The binding energies assigned to Sn $3d^{5/2}$ and Sn $3d^{3/2}$ of SnPO-IO_{288} were recognized at 487 eV and 495.5 eV, respectively, with the spin-orbit splitting of the doublet peaks of 8.5±0.1 eV (**Fig. 5a**). This binding energy confirms the existence of the Sn^{4+} cation in SnP_2O_7[34]. The binding energies assigned to the Sn $3d^{5/2}$ and Sn $3d^{3/2}$ regions show a slight change at 486.7 eV and 495.1 eV for SnPO-IO_{288}ca-MI. The binding energy spectrum of the P 2p region assigned for P from the PO_4 tetrahedra shows a similar slight shift of the peak from 133.5 eV for SnPO-IO_{288} to 133.3 eV for SnPO-IO_{288}ca-MI **(Fig. 5b)**. It can be predicted that the citric acid can protonate the surface via oxygen in the SnP_2O_7 lattice, as discussed in detail in the next part. The spectrum of the C1s region shows a strong peak at 284 eV assigned to the C=C bonding which comes from the decomposed products of polystyrene existing in SnPO-IO_{288} (**Fig. SI6**). The same result was analyzed for the binding energy of the O 1s region with a peak at 531 eV from the O-P bonding in both films, and extra peaks at 533 eV assigned to the O-C and O-H bonds for SnPO-IO_{288}ca-MI in the convolution spectrum (**Fig. SI6 and Tab. SI5**). The Cs^+ cation was almost not observed in the XPS spectrum of SnPO-IO_{288}ca-MI which confirmed the separation of the counter-cation from the cluster by using EPD. The binding energy spectrum of Mo 3d includes two specific peaks at 228.7eV ($3d^{5/2}$) and 231.8 eV ($3d^{3/2}$) which are assigned to the Mo-I bonding (**Fig. 5c**). The binding energy peak assigned to Mo-O (235.1) was not observed which means that the Mo_6 cluster does not oxidize or no valence bonding occurs between the cluster and other compositions [52]. The deconvolution spectra of I3d are presented in **Fig. 5d** that shows the peaks assigned to the inner iodine (I^i) at 620.1 eV ($3d^{5/2}$) and 631.6 eV ($3d^{3/2}$) and apical iodine (I^a) at 618.4 eV ($3d^{5/2}$) and 629.9 eV ($3d^{3/2}$). The average atomic ratio of I^i and I^a is 8 and 4 which was calculated from the deconvolution spectra of I3d (**Tab. SI6**). Based on the XPS analysis, the $[\{Mo_6I^i_8\}I^a_4[OH]^a_2]^{-2}$ cluster anions were suggested to move to the anode and be neutralized by the hydronium cation to form $[H_3O^+]_2[\{Mo_6I^i_8\}I^a_4[OH]^a_2]$ or $[\{Mo_6I^i_8\}I^a_4[H_2O]^a_2].yH_2O$ cluster compounds as

reported earlier [16]. Depending on the total Mo/I atomic ratio of 6/13.6 (theoretical index is 6:14), the separated iodine anions from the initial cluster were also deposited on an anode to form the iodide-enriched deposition. A similar conclusion has been revealed regarding the exchange of two apical ligands and the performance of the $[\{Mo_6Br^i_8\}Br^a_4[H_2O]^a_2].yH_2O$ film enriched Br anion layers which were prepared by EPD [53]. In summary, the acid modification successfully protonated the SnP_2O_7 lattice by hydrogen bonding that produced a slight shift in the binding energy of the Sn3d and P2p regions to the lower range. In addition, the general formula of the cluster in the film suggested being $[\{Mo_6I^i_8\}I^a_4[H_2O]^a_2].yH_2O$, possibly generating an interaction with the citric acid or SnP_2O_7 through the apical water ligands. This suggestion would support the electronic conducting transport in the material.

Based on the FT-IR spectrum of citric acid **(curve 1)**, the absorption peaks of the carbonyl (C=O) stretching vibration centered at 1759 and 1695 cm^{-1} shift to lower wavenumbers when citric acid is grafted on the SnP_2O_7 surface as shown in the spectrum of SnPO-IO_{288}ca (**curve 3**) (**Fig. 5e**). The covalent bond between a carboxylic group of the acid and oxygen on the surface of the SnP_2O_7 lattice can possibly be created by a thermal treatment, resulting in a shift of the absorption band of the carbonyl (C=O) stretching vibration. Besides, the wide absorption band in the 1700 and 1000 cm^{-1} range assigned to the O-H, C–O, C–OH, and C–C vibrations of the citric acid as well as the absorption bands in the 1300 and 400 cm^{-1} range assigned to the P-O and Sn-O vibration from the phosphate group **(curve 2)** in SnPO-IO_{288}ca were verified **(curve 3)**. Once the MI is immobilized on the IO film, the signal of C=O from the acid in SnPO-IO_{288}ca has an unchanged absorption band. It is suggested that the interaction that occurred between $[\{Mo_6I^i_8\}I^a_4[H_2O]^a_2]$ clusters and citric acid is hydrogen bonds (H-O…H) without covalent bonding. The chemical structure of MI has not changed after fabrication which can assure the retainment of the optical absorption characteristic in the visible domain.

Table **1.** The atomic concentration of the elements of SnPO-IO_{288} and SnPO-IO_{288}ca-MI by the peak analysis of the XPS measurements.

	Sn	O	C	P	Cs	Mo	I

	% at.							453
SnPO-IO$_{288}$	8.32	66.79	4.62	14.75	-	-	-	454
SnPO-IO$_{288}$ca-MI	8.86	56.91	10.67	14.51	-	2.91	6.56	455
								456

457

458

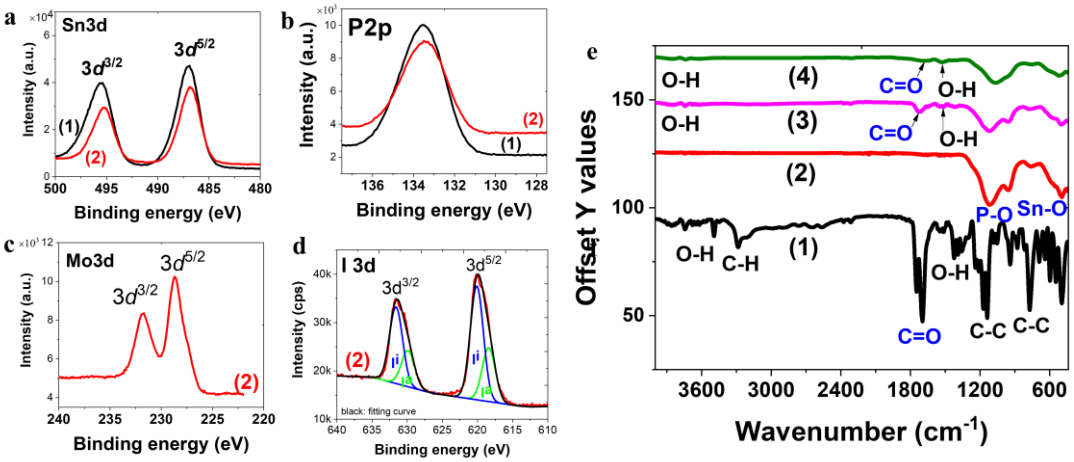

459

460 Figure 5. XPS binding energy (eV) spectra of SnPO-IO$_{288}$ **(1)** and SnPO-IO$_{288}$ca-MI **(2)**
461 including (a) Sn3d region, (b) P2p region, c) Mo3d region, and d) I3d region. (e) FTIR
462 spectra of citric acid (1), SnPO-IO$_{288}$ (2), SnPO-IO$_{288}$ca (3), and SnPO-IO$_{288}$ca-MI (4).

463 The specular reflectance spectra at the 5-degree incident angle of the SnPO-IO$_x$ca films
464 (x= 240, 288, 308 nm) from **Fig. SI7** confirm the stability of the ordered porous IO
465 structure after the citric acid treatment, showing relatively similar stopband peaks. In
466 order to confirm the different PBGs of the IO films before and after introducing the MI
467 cluster, the specular reflectance spectra of the IO films were performed (**Fig. 6a).** In **Figs.**
468 **4d and e**, the MI nanoparticles were anchored on the pore surface, and cluster
469 concentration was not enough to completely infiltrate the pores or make a thicker SnP_2O_7
470 wall. For this reason, the stop band peak for the SnPO-IO$_x$ca (x = 240, 288, 308 nm) films
471 still remains at a similar position to the original band structure after depositing the Mo_6
472 cluster. In general, the UV-Vis absorption spectrum of MI shows a strong UV-Vis light

absorption in the range between 300 and 550 nm and gradually reduces to 670 nm (**Fig. 6b**). The efficiency of the optical absorption of MI significantly linearly reduces from 400 and 600 nm after the MI deposited ITO substrate in comparison to the original powder (**Fig. 6c**). Besides the loss of Cs^+ cations, the exchange of iodine apical ligands during deposition from $[\{Mo_6I^i_8\}I^a_6]^{2-}$ to $[\{Mo_6I^i_8\}I^a_4[H_2O]^a_2].y\ H_2O$ also caused the reduction of visible light absorption of the Mo_6 cluster. The weak photoluminescence measured for the nanocomposite film shows a difference in comparison to that of the CMI powder (**Fig. SI8**). MI appeared to undergo a strong photoluminescence with an emission peak at 700 nm after creating a Mo-O covalent bonding with glycine and the layer double hydroxide as reported in a previous study [12]. In this study, the unchanged binding energy of Mo3d proves that the Mo atom of $[\{Mo_6I^i_8\}I^a_4[H_2O]^a_2].y\ H_2O$ does not create any covalent bonds with other compositions. However, it is well known that hydrolysis of the apical ligands of such a cluster complex leads to a small change in the luminescence spectra [54]. Although the composition modification occurred during fabrication, the CMI powder and MI-deposited ITO film still show the same optical absorption in the range from 400 to 600 nm with a different efficiency, resulting in a similar energy bandgap at 1.9 eV which is in agreement with the previous study [16].

The absorbance contribution of SnP_2O_7 in the visible light range is zero as seen in the disordered IO powder (dot line) from the transmittance spectrum of **Fig. 3c**. Therefore, the absorbance properties in the visible light of SnPO-IO_xca (x = 240, 288, 308) films will mainly assume the contributions of MI. (**Figs. 6c).** However, the cluster's visible light absorbing range of the Mo_6 cluster in the IO film is expanded to a higher wavelength than the MI-deposited ITO glass. The expansion wavelength range depends on the position of the stopband of the PBGs. The transmittance spectra also confirm the effect of the inverse opal which synergistically improves the light absorption around the original stopband (**Fig. 6d**). The SnPO-IO_xca-MI (x = 240, 288, 308) films show a transmittance of zero at various wavelengths which overlaps with the stop band from the IO structure of SnPO-IO_x even though there is no difference in the EPD parameter, substrate, and MI solution. The size of the MI nanoparticle is an average of 30 nm which is possible to be totally introduced inside 223, 267, and 294 nm-sized pores. The fact that the PBGs in the inverse opal structure are not able to enhance the light absorption because these photons will be

reflected in this frequency range. However, a slow photon effect that occurs on the stopband edges properly enhances the absorption of the material, leading to generating electron-hole pairs upon irradiation in these wavelength regions [24, 55]. Curti and colleagues have explained the behavior of the stopband and slow photons at different positions corresponding to the absorbance region of the material. Depending on their suggestion, PBGs at 379 nm and the slow photon effect are inactive because their wavelength is located within the region of the strong absorption of the Mo_6 cluster. In this case, there is no enhancement of photons for generating electron-hole pairs. On the other hand, the PBGs at 457 and 502 nm are inactive and their slow photon effects are active. When the stopband overlaps with the strong absorption region, the reflection will be avoided and the stopband band edges in the poor absorption region will enhance the light absorption in this range by slow photon effects. These phenomena are verified by an enhanced absorption part at higher wavelength ranges in **Fig. 6c**. The enhanced photon in the absorption region will be scattered inside the pore and absorbed by MI deposited within the IO structure to generate electron-hole pairs. In summary, the light utilization capability in the IO structure is improved due to slow photon-induced light absorption more reasonable than the photonic bandgap-induced light reflection. A few studies also reported that slow photons of the 3D inverse opal photonic crystals could promote light absorption of ZnO and TiO_2-Au-CdS for visible photocatalytic activity enhancement [55-57].

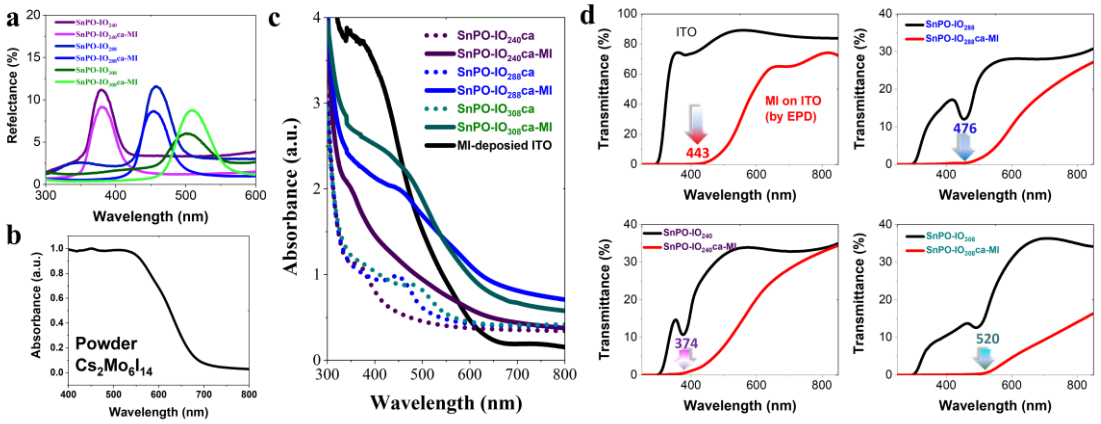

Figure 6. a) UV-vis absorbance spectra of CMI, b) the specular reflectance spectra at the 5-degree incident angle, c) UV-vis absorbance spectra and d) the transmittance spectra of

ITO glass, MI deposited on ITO glass and SnPO-IO_xca, and SnPO-IO_xca-MI (x = 240, 288, 308) films.

3.3 Effect of inverse opal structure on the photoconductivity response of Mo_6 cluster-functionalized SnP_2O_7 IO film

To understand the electrochemically kinetic information as well as the charge transport on the surface of the SnP_2O_7 bulk and MI cluster units, an illustration of the EIS measurement is presented in **Fig. SI9a.** The experiments were employed for the SnPO-IO_{288}, SnPO-IO_{288}ca, and SnPO-IO_{288}ca-MI films in the humidity and temperature-controlled chamber. The light will directly irradiate the cluster deposited IO film. The interfacial charge transfer resistance (R_{ct}) of the IO films measured at 298 K and 60 %RH was calculated from the fitted value by using a Randles equivalent circuit as depicted in **Fig. SI9b**. The charge transfer resistance (R_{ct}) of SnPO-IO_{288}ca was observed to be lower than that of SnPO-IO_{288} corresponding to the smaller semicircle from the Nyquist plots in **Fig. 7a**. In general, SnP_2O_7 nominally does not contain protons in the bulk which is proved by the disappearance of the O-H vibration as seen in the FT-IR spectra in the range between 3500 and 3000 cm^{-1} (**Fig. 3b**). However, SnP_2O_7 has been reported to exhibit a mixed proton and electron-hole conduction [39,40]. Therefore, the protonation process of SnP_2O_7 during modification in water has been discovered from reaction **(2):**

$$H_2O + O_o^x + 2h^{\cdot} \rightarrow 2OH_o^{\cdot} + 1/2O_2 \quad (2)$$

Where, O_o^x, $h^{\cdot}$ and $OH_o^{\cdot}$ denote a lattice oxide ion, an electron-hole, and a protonated lattice oxide ion, respectively.

The appearance of new protons with a high concentration in the SnP_2O_7 bulk was proved by the 1^H MAS NMR spectra reported by Shen et al. [32]. In addition, it was reported that protons migrate via dissociation of the O-H bond (hopping mechanism) [39]. At the humidity of 60% RH, protons coming from the water will interact with lattice oxide ions following reaction (2) to form a protonated lattice oxide ion on the surface of the SnP_2O_7 bulk. The introduction of citric acid supports the charge transport on the interface of the conducting IO film by a covalent bond with a protonated lattice oxide ion. It has been claimed that carboxylic acid self-assembled monolayers can reduce the band gap of the

initial work function that improves the device performance by aligning the energy levels in organic optoelectronic devices [51]. Moreover, citric acid contains two another carboxylic groups for generating hydrogen bonds on the SnP_2O_7 bulk surface which can accelerate the charge ion transport. As the result, the interfacial charge transport is improved in SnPO-IO_{288}ca. However, the deposition of $[\{Mo_6I^i_8\}I^a_4[H_2O]^a_2]\cdot yH_2O$ limited the transport of charge on the surface of the SnP_2O_7 bulk by blocking the hydroxyl groups by the hydrogen bond and made a significant increase in the interfacial charge transport resistance (R_{ct}) of more than 100 times.

However, only the SnPO-IO_{288}ca-MI interestingly shows the AC photoconductivity response with the photosensitivity of about 0.05±0.01 nS/cm and 0.10±0.01 nS/cm during the irradiation at fixed wavelengths in the UV range (350 and 370 nm) and visible range (410, 440, 540 and 580 nm), respectively (**Fig. 7b**). The photosensitivity in the visible light range (400-600 nm) is more efficient than in ultraviolet light. It can be explained that the photoconductivity response comes from the $[\{Mo_6I^i_8\}I^a_4[H_2O]^a_2]\cdot yH_2O$ clusters which strongly absorb in the visible range from 400 to 600 nm and generate photoexcited clusters containing an electron and a hole as already reported [16]. As is known, the $[\{Mo_6X^i_8\}X^a_6]^{2-}$ (X = halogen) cluster possesses a closed 24 valence electron shell. Some studies have demonstrated a reversible one-electron oxidation that leads to 23-electron complexes [58]. On the other hand, during the irradiation of photon energy, the MI cluster units will generate electron/hole pairs following reaction **(3)**. A hole on the photoexcited cluster will then react with water to form a proton followed by reaction **(4)** [12,59]**.**

$(Mo_6\ \text{cluster}) + h\nu \rightarrow (Mo_6\ \text{cluster})\ (h_{VB}^+, e_{CB}^-)$ (3)

$(Mo_6\ \text{cluster})\ (h_{VB}^+) + H_2O \rightarrow (Mo_6\ \text{cluster}) + {}^{\cdot}OH + H^+$ (4)

A schematic representation of the proton and electron conducting mechanism is illustrated in **Fig. 7c**. The Mo_6 clusters with apical water are anchored on the surface of SnP_2O_7 by a hydrogen bond with citric acid which is directly immobilized on SnP_2O_7. The separated electrons will move from the valence band to the conduction band and are collected by O-H bonding to move forward to SnP_2O_7 while the generated proton will continue to move inside the conducting SnP_2O_7 by hydrogen bonds and citric acid bridge.

585 Both electrons and protons, which result in a photoconductivity response, will add to the
586 total conductivity by transporting via the O-H bonds and protonated SnP_2O_7 bulk towards
587 the electrodes. When the illumination was switched off, the electron returned to the Mo_6
588 cluster and $OH^{\cdot}$ to form OH^- at the surface of SnP_2O_7. The conductivity of the MI film
589 prepared by EPD could not be measured due to the extremely low conductivity coming
590 from MI. As a result, the obtained conductivity of SnPO-IO_{288}ca-MI was essentially
591 contributed by SnP_2O_7 IO and the additive photocurrent comes from the contribution of
592 MI.

593 As is discussed, the protonic conductivity of SnP_2O_7 will be distributed by the water
594 concentration as seen in reaction **(2)**. **Figs. 7d and e,** respectively, present the dependence
595 of the conductivity on the relative humidity (RH) at 298K and the temperature at 80%
596 RH. The deposition of the Mo_6 cluster units does not influence the linear dependence of
597 the protonic and electrical conductivities on the environmental conditions. The activation
598 energy (E_a) was calculated from the relation with the ionic conductivity by E**q. 3**:

599 $\sigma T = A \cdot \exp(-E_a/RT)$ **(3)**

600 where A is a constant, T is the temperature, R is the gas constant, and E_a is the activation
601 energy. The slope of the fitted Arrhenius plots, wherein the value of the natural logarithm
602 of (σT) is linear versus the temperature (1/K), was used to calculate the activation energy
603 (**Fig. 7f**). The activation energy of SnPO-IO_{288}ca-MI is 0.39 eV that confirms the hopping
604 conduction mechanism [60].

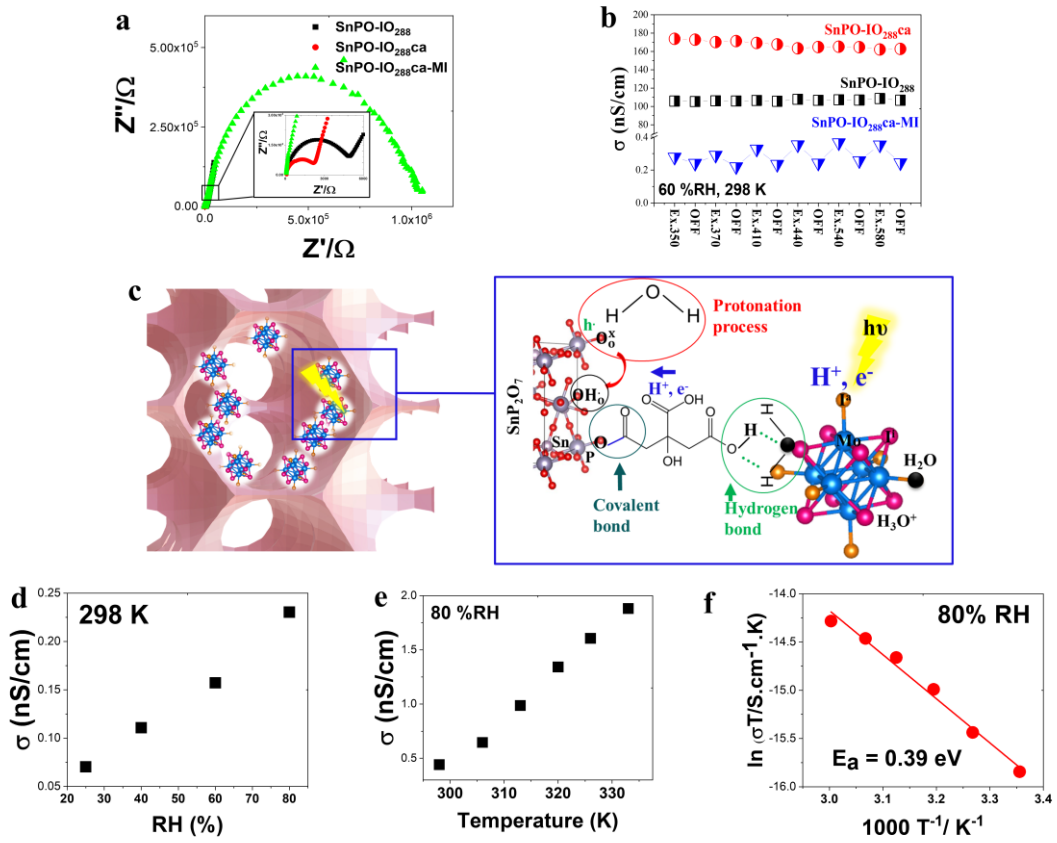

Figure 7. a) Nyquist plots of SnPO-IO$_{288}$, SnPO-IO$_{288}$ca, and SnPO-IO$_{288}$ca-MI at 298K and 60 %RH. (b) The AC photoconductivity response of the films at different irradiation wavelengths. c) Schematic representation of the proton and electron conducting mechanism between SnP_2O_7 and Mo_6 cluster. d) The dependence of the electrical conductivity vs. the relative humidity at 298 K, e) The dependence of the electrical conductivity vs. the temperatures at 80% RH, and f) Linear fits of the plots of ln (σT) versus T^{-1} of the thin films at different temperatures and humidities.

The IO structure with various pore sizes results in a different interfacial charge transport resistance (R_{ct}) during irradiation of different fixed wavelengths as seen in **Figs. 8 a,b, and c**. The thicknesses of the SnPO-IO$_{240}$ca-MI, SnPO-IO$_{288}$ca-MI, and SnPO-IO$_{308}$ca-MI films were respectively measured to be 4.9, 5.9, and 8.6 µm (**Fig. SI10**). It can be seen that R_{ct} decreases with a similar tendency for the films irradiated at wavelengths in the visible domain. SnPO-IO$_{308}$ca-MI has the lowest R_{ct} which means it produces the best photocurrent based on **Eq. 1**. The thickness and pore size will contribute to the humidity

absorption and the concentration of MI which influences the photocurrent. The increasing photoconductivity of the SnPO-IO_xca-MI (x = 240, 288, 308) films irradiated at the fixed wavelengths of 350, 370, 410, 440, 540, and 580 nm was calculated from **Eq. 1** (**Fig. 8d)**. All the films show the best increase in the photoconductivity response at the wavelengths of 410 and 440 nm, then a slight decrease at the wavelength of 580 nm. Several reasons have been considered for the photocurrent result such as i) the transmittance of the ITO glass in the UV range (70%) is lower than that in the visible range (>80%), and ii) the photon energy in the UV range is partially adsorbed by SnP_2O_7 (**Fig. 3c**). The reproducibility and photosensitization of the photoconductivity are important points for use in optical-related devices. The AC photocurrents of the films irradiated at the fixed wavelength of 580 nm were measured for 5 cycles with every measurement performed for 3 minutes without stopping (**Figs. 8e**). The photosensitization of SnPO-IO_{240}ca-MI, SnPO-IO_{288}ca-MI, and SnPO-IO_{308}ca-MI was, respectively, 0.034, 0.11, and 0.19 nS/cm irradiated at the wavelength of 580 nm. All the films obtained a good reproducibility of the photocurrent after 5 cycles of the EIS measurement. As seen in Fig. 8f, the deposited Mo_6 concentration is proportional to the thickness of the films which are determined by 0.14, 0.17, and 0.23 mg/cm^2 corresponding to the thickness value at 4.9, 5.9, and 8.6 µm, respectively, for SnPO-IO_{240}, SnPO-IO_{288}, and SnPO-IO_{308}. For the same EPD parameters, the bigger the PS bead size, the larger the pore size, and the thicker the IO film. During EPD, the charged PS particles smoothly move toward the IO electrode within a greater pore volume, resulting in more Mo_6 clusters in thicker IO film. Moreover, the incidence light will be reflected at the stopband while the absorption light will be enhanced at the stopband edges by an impact of slow photons which occur for the poor absorption region. As is discussed in **Fig. 6**, only the films which show the PBGs at 457 and 502 nm can activate a low photon effect. The enhanced absorbance light will be mostly scattered within the pore and adsorbed by the Mo_6 cluster (**Fig. 8g**). Moreover, the scattering light will be proportionally enhanced with the increase in the macropore size. As the result, the IO film containing PBG at 502 nm that its stopband edge overlaps with to excitation wavelength at 580 nm can show the highest ability to generate electron-hole pairs for increasing the photocurrent upon illumination at this wavelength. In summary, the baseline current will be affected by the thickness of SnP_2O_7, while the

photocurrent depends on the MI concentration controlled by the thickness, active porous areas, and the slow photon effect in the stopband edges.

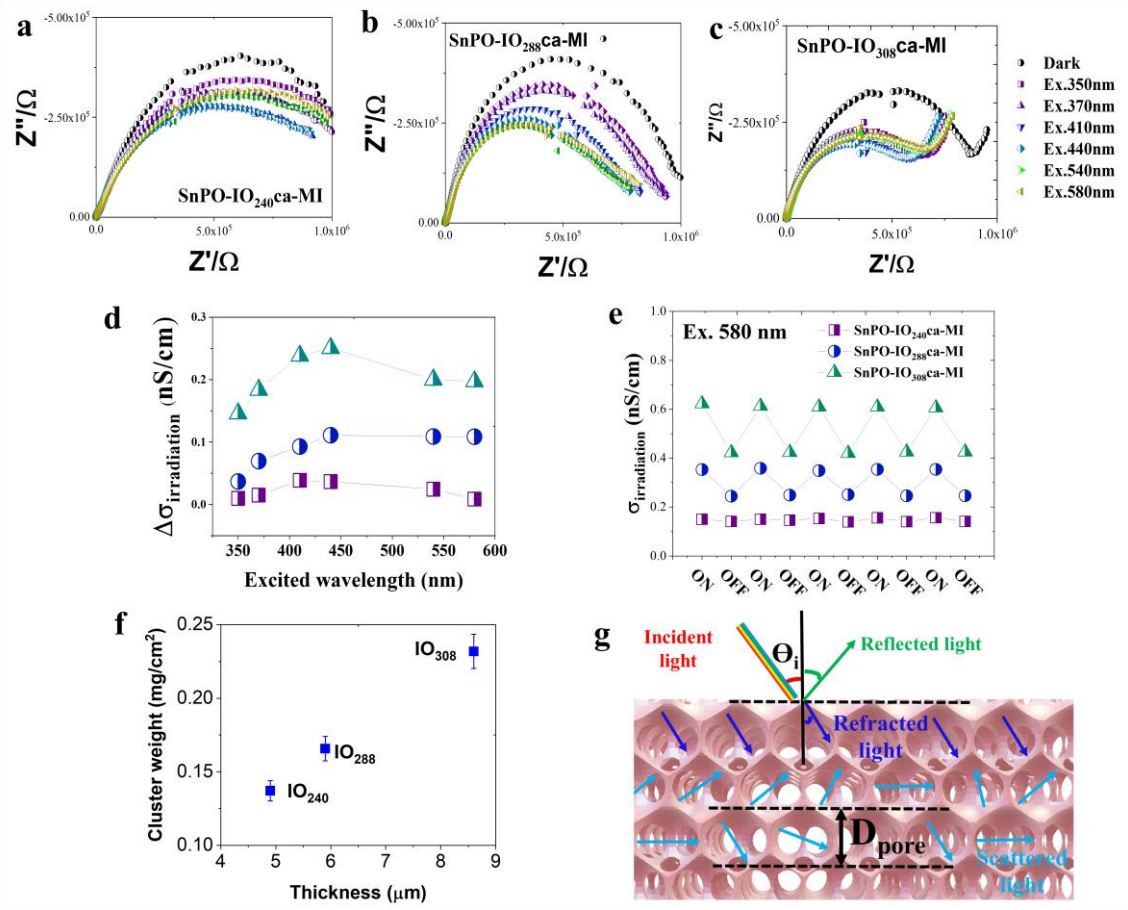

Figure 8. Nyquist plots of (a) SnPO-IO_{240}ca-MI, (b) SnPO-IO_{288}ca-MI, and (c) SnPO-IO_{308}ca-MI films. d)The AC photoconductivity response of SnPO-IO_xca-MI (x = 240, 288, 308) films at different excitation wavelengths at 297K and RH 60%. e) Repeatability of photoconductivity response of SnPO-IO_xca-MI (x = 240, 288, 308) films irradiated at the fixed wavelength of 580 nm. F) Schematic illustration of the absorption light scattered by the IO structure.

The reproducible on/off switching curves of the DC photocurrent at the bias voltage of the 0.5 V of SnPO-IO_xca-MI (x = 288, and 308) films are presented in **Figs. 9a and b,** respectively. The measurement of SnPO-IO_{240}ca-MI was skipped in this experiment because the slow photon effect does not occur at the stopband edge of PBG. It is noted that the DC photoconductivity responses depend on light illumination at the wavelengths

of 440, 540, and 580 nm at the relative humidity (RH) of 80% and 298 K. The photocurrents from various excitation wavelengths have different baselines due to currents that are not stable after a continual and long measurement time. The excitation light at wavelengths, which overlapped with the stopband edges of PBG results in a leading light absorption in these wavelengths. This would explain the highest observed photocurrents; the slow photon effect occurs around PBG at 453 nm of the SnPO-IO_{288}ca-MI which is near the irradiation light of 440 nm (Fig. 9a), whereas SnPO-IO_{308}ca-MI shows a slow photon somewhere closer to 540 nm (Fig. 9b). Both films with different pore sizes result in a stable photocurrent reproducibility after 15 cycles. Reproducible on/off switching curves at the 580 nm illumination of the nanocomposite films measured at different humidities and 298 K are shown in **Fig. 9c and Fig. SI11**. The photocurrent response is proportional to the relative humidity which agreed with **Fig. 7d** following the hopping conduction mechanism. At the temperature of 298K and RHs of 30%, 60%, and 80%, the photosensitive of SnPO-IO_{308}ca-MI was recognized to be about 0.11, 1.29, and 2.41 nA/cm^2 during the irradiation of the fixed wavelengths at 580 nm, respectively. Humidity plays an essential role to provide a water carrier that accelerates the movement of ions and electrons. In addition, the photocurrent also shows a linear dependence on the illumination power (**Fig. 9d**). The rising and decaying photocurrent responses (τ) were measured at 0.1 and 0.2 s, indicating a rapid photoresponse characteristic (**Fig. 9e**). The reproductivity of the photoconductivity was also obtained in a short time that improved in comparison to the layer double hydroxides functionalized by MI clusters in a previous report [12]. This result is more interesting for the application of environmental sensors or visible photodetectors.

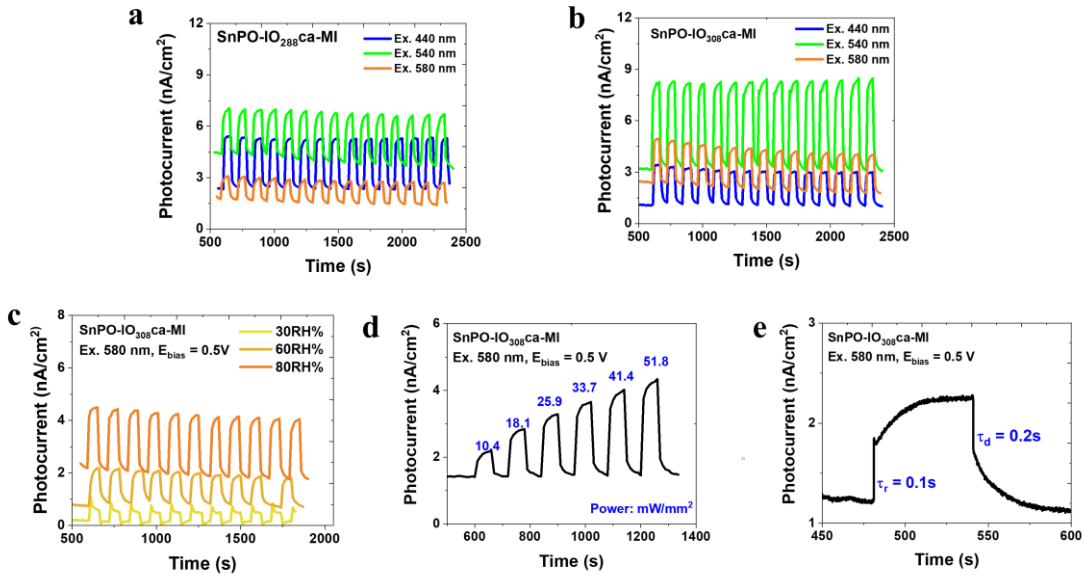

Figure 9. Reproducible on/off switching curves of DC photocurrent at a bias voltage of 0.5 V of a) the SnPO-IO_{288}ca-MI film and b) SnPO-IO_{308}ca-MI film during the illumination by different light wavelengths measured at RH of 80 % and 298 K versus the time, and c) SnPO-IO_{308}ca-MI film during the illumination by the wavelengths of 580 nm measured at different humidities and 298 K versus the time. d) The DC photocurrent of the SnPO-IO_{308}ca-MI film during the illumination by the wavelengths of 580 nm measured at the RH of 80%, 298 K, and different powers versus irradiation power. e) Enlarged rising and decaying edges of the photocurrent response of the SnPO-IO_{308}ca-MI film (298 K, 80 %RH) during the illumination of power at the 51.8 mW/mm^2.

A good photosensitization and reproducibility depend on the interfacial charge transport which is contributed by the protonic and electrical conductivities coming from the Mo_6 cluster, SnP_2O_7, and an acid bridge between them. The proton conductivity of three molybdenum cluster-based materials as building blocks, $(H)_4[Mo_6Br_6S_2(OH)_6]$-$12H_2O$ and $(H)_2[Mo_6X_8(OH)_6]$-$12H_2O$ (X = Cl, Br), was reported for the first time with the good conductivity of 1.4×10^{-4} $S \cdot cm^{-1}$ under wet conditions for $(H)_2[Mo_6Cl_8(OH)_6]$-$12H_2O$ (X = Cl, Br) [61]. It is possibly claimed that concerted proton transfers through the hydrogen-bond network and vehicular (or diffusion) transport probably occur within the materials. During the irradiation, it was proved that the excited electron enhanced the charge on the surface of the Mo_6 cluster and was easily transported in the network [15].

The covalent and hydrogen bonds generated between the Mo_6 cluster with graphene oxide, silica oxide, hexagonal boron nitride, and layered double hydroxide have been reported that achieved an excellent photooxidation for a catalyst and photocurrent for optoelectronic materials [12, 62-64]. Hence, the strategy for the improvement of this material in the future is to find a new approach for improving the photon and electrical photoconductivity of the SnP_2O_7 IO films by doping some different metals, such as In, Al, and Mg elements, and creating covalent bonding with the Mo_6 cluster.

4. CONCLUSIONS

For the first time, the 3D SnP_2O_7 conducting inverse opals with different pore size intergrated Mo_6 clusters were successfully fabricated by electrophoretic deposition and thermal treatment. The acid surface modification of the SnP_2O_7 IO films results in an improvement of the deposited concentration of the Mo_6 cluster. The covalent bonding was recognized between the citric acid and SnP_2O_7 IO films by FTIR and XPS. The $[\{Mo_6I^i_8\}I^a_4[H_2O]^a_2].yH_2O$ cluster compound still retained the octahedral structure with a poor existence of Cs^+ counter-cations and exchanging of the two apical iodide ligands compared to the $Cs_2[\{Mo_6I^i_8\}I^a_6]$ precursor. The SnP_2O_7 IO films exhibited PBG at 379, 457, and 502 nm, and their stopband edges activated the slow photon effect to enhance the optical adsorbing property of the Mo_6 cluster. Interestingly, the photocurrent response during the irradiation of visible light with a high photosensitivity efficiency comes from the Mo_6 cluster-functionalized SnP_2O_7 IO films. The protons and electrons conducting mechanism of the SnP_2O_7 IO films combines the proton and electrical conductivities via hydrogen bonding (a vehicular mechanism). The reproducibility and photostability of the nanocomposite were confirmed by both EIS measurement and DC measurement. This study will contribute to the achievement of the nanocomposite family that can show an efficient photoconductivity response in the visible domain, an important characteristic of materials for applications of water splitting, photodetectors, and photoelectrodes for dye-sensitized solar cells.

AUTHOR CONTRIBUTIONS

Thi Kim Ngan Nguyen conceived and designed the experiments; performed the experiments, analyzed and interpreted the data, and drafted the article. Fabien Grasset and Stephane Cordier analyzed and interpreted the data; and drafted the article. Noee Dumait performed the experiments. Satoshi Ishii, Hiroshi Fudouzi, and Tetsuo Uchikoshi critically revised to improve the intellectual content.

ACKNOWLEDGMENTS

These studies were carried out as part of the France-Japan International Collaboration Framework (IRL3629 LINK) with the partial support of Dr. David Berthebaud as director. T.K.N. Nguyen thanks to the International Center for Young Scientists (ICYS-Sengen) and NIMS for the continued financial support. I would like to thank Prof. Naoto Shirahata for his useful advice and Dr. Cédric Bourgès for his XRD analysis.

APPENDIX A. SUPPLEMENTARY MATERIAL

Supplementary data to this article can be found online at

REFERENCES

[1] A. Chetia, J. Bera, A. Betal, S. A. Sahu, brief review on photodetector performance based on zero-dimensional and two dimensional materials and their hybrid structures. Materials Today Communications, 30 (2022) 103224. https://doi.org/10.1016/j.mtcomm.2022.103224.

[2] B. Ezhilmaran, A. Patra, S. Benny, M. R. Sreelakshmi, V. V. S.Akshay, S. Venkataprasad Bhat, C.S. Rout, Recent developments in the photodetector applications of Schottky diodes based on 2D materials. J. Mater. Chem. C, 9 (2021) 6122-6150. https://doi.org/10.1039/D1TC00949D

[3] F. S. Liang, S. J. Wang, S. P. Li, L. B. Luo, Near-Infrared-Light Photodetectors Based on One-Dimensional Inorganic Semiconductor Nanostructures. Advanced Optical Materials, 5 (2017) 1700081. https://doi.org/10.1002/adom.201700081

[4] M. Manikandan, D. Nirmal, J. Ajayan, B. Mohankumar, P. Prajoon, L. Arivazhagan, A review of blue light emitting diodes for future solid state lighting and visible light

763 communication applications. Superlattices and Microstructures. 136 (2019) 106294.
764 https://doi.org/10.1016/j.spmi.2019.106294
765 [5] A. Minotto, P. A. Haigh, L. G. Łukasiewicz, E. Lunedei, D. T. Gryko, I. Darwazeh,
766 F. Cacialli, Visible light communication with efficient far-red/near-infrared polymer
767 light-emitting diodes. Light Sci. Appl., 9 (2020) 70-81. https://doi.org/10.1038/s41377-
768 020-0314-z
769 [6] K. Kirakci, S.Cordier, C. Perrin, Synthesis and Characterization of $Cs_2Mo_6X_{14}$ (X =
770 Br or I) Hexamolybdenum Cluster Halides: Efficient Mo_6 Cluster Precursors for Solution
771 Chemistry Syntheses. Z. Anorg. Allg. Chem., 63 (2005) 411-416.
772 https://doi.org/10.1002/zaac.200400281
773 [7] B. Dierre, K. Costuas, N. Dumait, S. Paofai, M. Amela-Cortes, Y. Molard, F. Grasset,
774 Y. Cho, K. Takahashi, N. Ohashi, T. Uchikoshi, S. Cordier. Mo_6 cluster-based
775 compounds for energy conversion applications: comparative study of photoluminescence
776 and cathodoluminescence. Sci. Technol. Adv. Mater., 181 (2017) 458-466.
777 DOI: 10.1080/14686996.2017.1338496
778 [8] M. Prévôt, M. Amela-Cortes, S.K. Manna, R. Lefort, S. Cordier, H. Folliot, L. Dupont,
779 Y. Molard, Design and Integration in Electro-Optic Devices of Highly Efficient and
780 Robust Red-NIR Phosphorescent Nematic Hybrid Liquid Crystals Containing
781 $[Mo6I8(OCOCnF2n_{+1})_6]^{2-}$(n = 1, 2, 3) Nanoclusters. Adv. Funct. Mater, 25 (2015)
782 4966–4975. https://doi.org/10.1002/adfm.201501876
783 [9] P. S. Kuttipillai, Y. Zhao, C. J. Traverse, R. J. Staples, B. G. Levine, R. R. Lunt,
784 Phosphorescent Nanocluster Light-Emitting Diodes. Adv. Mater., 18 (2016) 320–326.
785 https://doi.org/10.1002/adma.201504548
786 [10] E. F. Molina, N. A. Martins de Jesus, S.Paofai, P. Hammer, M. Amela-Cortes, M.
787 Robin, S. Cordier, Y.Molard, When a Red–NIR-Emissive $Cs_2[Mo_6Br_{14}]$ Interacts with
788 an Active Diureasil–PEO Matrix: Design of Tunable and White-Light-Emitting Hybrid
789 Material. Chem. Eur. J., 25 (2019) 15248 – 15251.
790 https://doi.org/10.1002/chem.201903892
791 [11] T. K. N. Nguyen, A. Renaud, M. Wilmet, N. Dumait, S. Paofai, B. Dierre, W.Chen,
792 N. Ohashi, S. Cordier, F.Grasset, T. Uchikoshi, New ultraviolet and near-infrared
793 blocking filters for energy saving applications: fabrication of tantalum metal atom cluster-

794 based nanocomposite thin films by electrophoretic deposition. J. Mater. Chem. C, 5
795 (2017)10477-10484. https://doi.org/10.1039/C7TC02454A
796 [12] T. K. N. Nguyen, N. Dumait, F. Grasset, S. Cordier, D. Berthebaud, Y. Matsui,
797 N.Ohashi, T.Uchikoshi, Zn−Al Layered Double Hydroxide Film Functionalized by a
798 Luminescent Octahedral Molybdenum Cluster: Ultraviolet−Visible Photoconductivity
799 Response. ACS Applied Materials & Interfaces, 12 (2020) 40495-40509. https://doi.org/
800 10.1021/acsami.0c10487ff. ffhal-02930344
801 [13] A. Renaud, T.K.N. Nguyen, F. Grasset, M. Raissi, V. Guillon, F. Delabrouille, N.
802 Dumait, P. Y. Jouan, L. Cario, S. Jobic, Y. Pellegrin, F. Odobel, S. Cordier, T. Uchikoshi,
803 Preparation by electrophoretic deposition of molybdenum iodide cluster-based functional
804 nanostructured photoelectrodes for solar cells. Electrochimica Acta, 17 (2019) 37-745.
805 https://doi.org/10.1016/j.electacta.2019.05.154
806 [14] M. Feliz, P. Atienzar, M. Amela-Cortés, N. Dumait, P. Lemoine, Y. Molard,
807 S.Cordier, Supramolecular Anchoring of Octahedral Molybdenum Clusters onto
808 Graphene and Their Synergies in Photocatalytic Water Reduction. Inorganic Chemistry,
809 58 (2019)15443-15454. https://doi.org/10.1021/acs.inorgchem.9b02529
810 [15] K. Harada, T. K. N. Nguyen, F. Grasset, C. Comby-Zerbino, L. MacAleese, F.
811 Chirot, P. Dugourd, N. Dumait, S. Cordier, N. Ohashi, M. Matsuda, T. Uchikoshi, Light-
812 dependent ionic-electronic conduction in an amorphous octahedral molybdenum cluster
813 thin film. NPG Asia Mater., 14 (2022) 21. https://doi.org/10.1038/s41427-022-00366-8
814 [16] A. Renaud, P. V. Jouan, N. Dumait, S. Ababou-Girard, N. Barreau, T. Uchikoshi, F.
815 Grasset, S. Jobic, S. Cordier, Evidence of the Ambipolar Behavior of Mo_6 Cluster Iodides
816 in All-Inorganic Solar Cells: A New Example of Nanoarchitectonic Concept. ACS
817 Applied Materials & Interfaces, 14 (2022) 347-1354.
818 https://doi.org/10.1021/acsami.1c17845
819 [17] S. Khlifi, J. Bigeon, M. Amela-Cortes, N. Dumait, G. Loas, S. Cordier, Y.Molard,
820 Switchable Two-Dimensional Waveguiding Abilities of Luminescent Hybrid
821 Nanocomposites for Active Solar Concentrators. ACS Applied Materials & Interfaces, 12
822 (2020)14400-14407. https://doi.org/10.1021/acsami.9b23055
823 [18] M. Shkir, M. T. Khan, I. M. Ashraf, A. Almohammedi, E. Dieguez, S. AlFaify, High-
824 performance visible light photodetectors based on inorganic CZT and InCZT single

825 crystals. Scientific Reports, 9 (2019) 12436. https://doi.org/10.1038/s41598-019-48621-
826 3
827 [19] P. H. Chung, C. T. Kuo, T. H.Wang, Y. Y. Lu, C. I. Liu, T.R. Yew. A Sensitive
828 Visible Light Photodetector Using Cobalt-Doped Zinc Ferrite Oxide Thin Films, ACS
829 Appl. Mater. Interfaces, 13 (2021) 6411–6420. https://doi.org/10.1021/acsami.0c20487
830 [20] S. Yanikgonul, V. Leong, J. R.Ong, T.Hu, S. Y. Siew, C. E. Png. L.Krivitsky,
831 Integrated avalanche photodetectors for visible light. Nature Communications,12
832 (2021)1834. https://doi.org/10.1038/s41467-021-22046-x
833 [21] T. Ji, Q. Liu, R. Zou, Y.Zhang, L. Wang, L. Sang, M. Liao, J.Hu, Enhanced UV-
834 visible light photodetectors with a TiO_2/Si heterojunction using band engineering. J.
835 Mater. Chem. C, 5 (2017) 12848-12856. https://doi.org/10.1039/C7TC04811D
836 [22] E. Armstrong, C. O'Dwyer, Artificial opal photonic crystals and inverse opal
837 structures – fundamentals and applications from optics to energy storage. J. Mater. Chem.
838 C, 3 (2015) 109-1143. DOI https://doi.org/10.1039/C5TC01083G
839 [23] C. I. Aguirre, E. Reguera, and A. Stein, Tunable Colors in Opals and Inverse Opal
840 Photonic Crystals, Adv. Funct. Mater., 20 (2010) 2565–2578
841 https://doi.org/10.1002/adfm.201000143
842 [24] M. Curti, J. Schneider, D. W. Bahnemann, C. B. Mendive, Inverse Opal Photonic
843 Crystals as a Strategy to Improve Photocatalysis: Underexplored Questions, J. Phys.
844 Chem. Lett., 6 (2015) 3903−3910, https://doi.org/10.1021/acs.jpclett.5b01353

845 [25] Y. Gun, G. Y. Song, V. H. V. Quy, J. Heo, H. Lee, K.S. Ahn, S. H. Kang, Joint
846 Effects of Photoactive TiO2 and Fluoride-Doping on SnO2 Inverse Opal
847 Nanoarchitecture for Solar Water Splitting, ACS Appl. Mater. Interfaces, 7 (2015)
848 20292−20303 https://doi.org/10.1021/acsami.5b05914

849 [26] F. Temerov, K. Pham, P. Juuti, J. M. Makela, E. V. Grachova, S. Kumar, S. Eslava,
850 J. J. Saarinen, Silver-Decorated TiO_2 Inverse Opal Structure for Visible Light- Induced
851 Photocatalytic Degradation of Organic Pollutants and Hydrogen Evolution, ACS Appl.
852 Mater. Interfaces, 12 (2020) 41200−41210 https://doi.org/10.1021/acsami.0c08624

[27] L. Zhang, E. Reisner, J. J. Baumberg, Al-doped ZnO inverse opal networks as efficient electron collectors in BiVO4 photoanodes for solar water oxidation, Energy Environ. Sci., 7 (2014)1402–1408 https://doi.org/10.1039/C3EE44031A

[28] J. Wang, Y. Yuan, H. Zhu, T. Cai, Y. Fang, O. Chen, Three-dimensional macroporous photonic crystal enhanced photon collection for quantum dot-based luminescent solar concentrator, Nano Energy, 67 (2020) 104217. https://doi.org/10.1016/j.nanoen.2019.104217

[29] D.Gaillot, T. Yamashita, C. J. Summers, Photonic band gaps in highly conformal inverse-opal based photonic crystals. Physical Review B, 2 (2005) 205109. https://doi.org/10.1103/PhysRevB.72.205109

[30] Z. Cai, Y. Yan, L. Liu, S. Lin, H.Hu, Controllable fabrication of metallic photonic crystals for ultra-sensitive SERS and photodetectors. RSC Adv., 7 (2017) 5851–55858. https://doi.org/10.1039/C7RA11721C

[31] K. Xie, M. Guo, H.Huang, Photonic crystals for sensitized solar cells: fabrication, properties, and applications. J. Mater. Chem. C, 3 (2015) 10665-10686. https://doi.org/10.1039/C5TC02121A.

[32] Y. Shen, M. Nishida, W. Kanematsu, T. Hibino, Synthesis and characterization of dense SnP_2O_7–SnO_2 composite ceramics as intermediate-temperature proton conductors. Journal of Materials Chemistry, 21 (2011) 663–670. https://doi.org/10.1039/C0JM02596H

[33] K. S. Lee, S. Maurya, Y. S. Kim, C. R. Kreller, M. S. Wilson, D. Larsen, S. E. Elangovan, R.Mukundan, Intermediate temperature fuel cells via an ion-pair coordinated polymer electrolyte. Energy Environ. Sci., 1 (2018) 979-987. https://doi.org/10.1039/C7EE03595K

[34] K. P. Ramaiyan, S.Herrera, M. J. Workman, T. A. Semelsberger, V. Atanasov, J. Kerres, S. Maurya, Y. S. Kim, C. R. Kreller, R.Mukundan, Role of phosphate source in improving the proton conductivity of tin pyrophosphate and its electrolytes. J. Mater. Chem. A, 2020, 8, 16345-16354. https://doi.org/10.1039/D0TA04327C

[35] J. Pan, S. Chen, D. Zhang, S.Xu, Y. Sun, F. Tian, P. Gao, J. Yang, SnP_2O_7 Covered Carbon Nanosheets as a Long-Life and High-Rate Anode Material for Sodium-Ion

884 Batteries. Advanced Functional Materials, 2018, 28, 1804672.
885 https://doi.org/10.1002/adfm.201804672
886 [36] I. Bezzaa, V. Trouillet, A. Fiedler, M. Bruns, S. Indris, H. Ehrenberg, I. Saadoune,
887 Understanding the lithiation/delithiation process in SnP_2O_7 anode material for lithium-
888 ion batteries. Electrochimica Acta, 252 (2017) 446–452.
889 https://doi.org/10.1016/j.electacta.2017.09.023
890 [37] P.Lv, T. Ito, A. Oogushi, K. Nakashima, M. Nagao, T. A Hibino, self-regenerable
891 soot sensor with a proton-conductive thin electrolyte and a nanostructured platinum
892 sensing electrode. Sci. Rep., 6 (2016) 37463. https://doi.org/10.1038/srep37463
893 [38] J. Zhong, C. Li, W. Zhao, S. You, J. Brgoch, Accessing High-Power Near-Infrared
894 Spectroscopy Using Cr^{3+} -Substituted Metal Phosphate Phosphors. Chemistry of
895 Materials, 34 (2022) 337-344. https://doi.org/10.1021/acs.chemmater.1c03671
896 [39] M. Nagao, T. Kamiya, P. Heo, A.Tomit, T. Hibino, M. Sanoa, Proton Conduction in
897 In^{3+} Doped SnP_2O_7 at Intermediate Temperatures. Journal of The Electrochemical
898 Society, 53 (2006) 604-1609. https://doi.org/10.1149/1.2210669
899 [40] H. Wang, J. Xiao, Z. Zhou, F. Zhang, H. Zhang, G. Ma, Ionic conduction in undoped
900 SnP_2O_7 at intermediate temperatures. Solid State Ionics, 81 (2010), 1521–1524.
901 https://doi.org/10.1016/j.ssi.2010.08.029
902 [41] J. F. Dechezelles, T. Aubert, F. Grasset, S. Cordier, C. Barthou, C. Schwob, A.
903 Maıtre, R. A. L. Vallee, H. Cramaild, S. Ravaine, Fine tuning of emission through the
904 engineering of colloidal crystals Phys. Chem. Chem. Phys., 12 (2010), 11993–11999
905 https://doi.org/10.1039/C0CP00129E
906 [42] A. Renaud, F. Grasset, B. Dierre, T. Uchikoshi, N. Ohashi, T. Takei, A. Planchat, L.
907 Cario, S. Jobic, B.Odobel, S. Cordier, Inorganic Molybdenum Clusters as Light-
908 Harvester in All Inorganic Solar Cells: A Proof of Concept, Chemistry Select, 1 (2016),
909 2284-2289 https://doi.org/10.1002/slct.201600508
910 [43] S. Furumi, H. Fudouzi, T. Sawadaa, Dynamic photoswitching of micropatterned
911 lasing in colloidal crystals by the photochromic reaction. J. Mater. Chem., 2 (2012),
912 21519–21528. https://doi.org/10.1039/C2JM34747D
913 [44] T. Roisnel, J. Rodriguez-Carvajal, WinPLOTR: a Windows tool for powder
914 diffraction patterns analysis, Materials Science Forum, Ed. R. Delhez and E.J.
915 Mittenmeijer, 378-381 (2001) 118-123.

[45] J. Rodríguez-Carvajal, Recent Developments of the Program FULLPROF, Newsletter in Commission on Powder Diffraction (IUCr), 2001, 26, 12.

[46] K. Katagiri, Y. Tanaka, K. Uemura, K. Inumaru, T.Seki, Y.Takeoka, Structural color coating films composed of an amorphous array of colloidal particles via electrophoretic deposition. Npg Asia Materials, 9 (2017) 355-362. https://doi.org/10.1038/am.2017.13

[47] F. Fayon, I. J. King, R. K. Harris, R. K. B. Gover, J. S. O. Evans, D.Massiot, Characterization of the Room-Temperature Structure of SnP_2O_7 by 31P Through-Space and Through-Bond NMR Correlation Spectroscopy. Chem. Mater., 5 (2003) 2234-2239. https://doi.org/10.1021/cm031009d

[48] L. Kőrösi, S. Papp, V. Meynen, P. Cool, E. F. Vansant, I. Dékány, Preparation and characterization of SnO_2 nanoparticles of enhanced thermal stability: The effect of phosphoric acid treatment on $SnO_2 \cdot nH_2O$. Physicochemical and Engineering Aspects, 268 (2005) 147-154. https://doi.org/10.1016/j.colsurfa.2005.05.074

[49] H. Wang, J. Xiao, Z. Zhou, F.Zhang, H.Zhang, G. Ma, Ionic conduction in undoped SnP_2O_7 at intermediate temperatures. Solid State Ionics, 2010, 81, 1521–1524.

[50] A. Richel, N. P. Johnson and D. W. McComb Observation of Bragg reflection in photonic crystals synthesized from air spheres in a titania matrix Appl. Phys. Lett. 76, 1816 (2000); https://doi.org/10.1063/1.126175

[51] N. Kramer, S. Sarkar, L. Kronik, N.Ashkenasy, Systematic modification of the indium tin oxide work function via side-chain modulation of an amino-acid functionalization layer. Phys.Chem.Chem.Phys., 21 (2019) 21875-21881. https://doi.org/10.1039/C9CP04079J

[52] T. K. N. Nguyen, Y. Matsuia, N. Shirahata, N. Dumait, S. Cordier, F.Grasset, N. Ohashi, T.Uchikoshi, Zn-Al layered double hydroxide-based nanocomposite functionalized with an octahedral molybdenum cluster exhibiting prominent photoactive and oxidation properties. Applied Clay Science, 96 (2020) 105765. https://doi.org/10.1016/j.clay.2020.105765

[53] T. K. N. Nguyen, B. Dierre, F. Grasset, A. Renaud, S. Cordier, P. Lemoine, N. Ohashi, T. Uchikoshi, Formation Mechanism of Transparent Mo6 Metal Atom Cluster Film Prepared by Electrophoretic Deposition. Journal of The Electrochemical Society, 164 (2017) 412-418. https://doi.org/10.1149/2.0591707jes

[54] M. V. Marchuk, N. A. Vorotnikova, Y. A. Vorotnikov, N. V. Kuratieva, D. V. Stass, and M. A. Shestopalov, Optical property trends in a family of {Mo6I8} aquahydroxo complexes, Dalton Trans., 2021, 50, 8794–8802. https://doi.org/10.1039/D1DT01293B

[55] J. Liu, J. Jin, Y. Li, H.W. Huang, C. Wang, M. Wu, L.-H. Chen and B.-L. Su, Tracing the slow photon effect in a ZnO inverse opal film for photocatalytic activity enhancement, J. Mater. Chem. A, 2 (2014) 5051–5059, DOI: 10.1039/c3ta15044e

[56] H. Zhao, Z. Hua, J.Liu, Y.Li, M.Wu, G. V. Tendeloo, B.-L. Suade, Blue-edge slow photons promoting visible-light hydrogen production on gradient ternary 3DOM TiO2-Au-CdS photonic crystals, Nano Energy, 47 (2018) 266-274, DOI: 10.1016/j.nanoen.2018.02.052

[57] Z. Li, S. Feng, Y. Liu, J. Hu, C. Wang, B. Wei, Enhanced Tunable Light Absorption In Nanostructured Si Arrays Based On Double-Quarter-Wavelength Resonance, Adv. Opt. Mater., 7 (2019) 1900845, DOI: 10.1002/adom.201900845

[58] N. A. Vorotnikova, Y. A. Vorotnikov, I. N. Novozhilov, M. M. Syrokvashin, V. A. Nadolinny, N. V. Kuratieva, D. M. Benoit, Y. V. Mironov, R. I. Walton, G. I. Clarkson, N.Kitamura, A. J. Sutherla, M. A. Shestopalov, P. A. Efremova, $^{23-}$Electron Octahedral Molybdenum Cluster Complex $[\{Mo_6I_8\}Cl_6]^{-}$. Inorg. Chem., 57 (2018) 811−820. https://doi.org/10.1021/acs.inorgchem.7b02760

[59] P. Kumar, H.P. Mungse, S. Cordier, R. Boukherroub, O. P. Khatri, S. L. Jain, Hexamolybdenum clusters supported on graphene oxide: Visible-light Induced Photocatalytic Reduction of Carbon Dioxide Into Methanol. Carbon, 94 (2015) 91-100. https://doi.org/10.1016/j.carbon.2015.06.029

[60] K. D. Kreuer, A. Rabenau, W.Weppner, Vehicle Mechanism, A New Model for The Interpretation of The Conductivity of Fast Proton Conductors, Angew. Chem. Int. Ed. Engl., 21 (1982) 208-209. https://doi.org/10.1002/anie.198202082

[61] G. Daigre, J.Cuny, P. Lemoine, M. Amela-Cortes, S. Paofai, N.Audebrand, A. L. G. L. Salle, E. Quarez, O.Joubert, N. G. Naumovand, S.Cordier, Metal Atom Clusters as Building Blocks for Multifunctional Proton- Conducting Materials: Theoretical and ExperimentalCharacterization. Inorg. Chem., 7 (2018), 814−9825. https://doi.org/10.1021/acs.inorgchem.8b00340

977 [62] A. Barras, M. A. Das, R. R. Devarapalli, M. V. Shelkec, S. Cordier, S. Szunerits, R.
978 Boukherroub, One-pot synthesis of gold nanoparticle/molybdenum cluster/graphene
979 oxide nanocomposite and its photocatalytic activity. Appl. Catalysis B: Environmental,
980 30– 131 (2013) 70– 276. https://doi.org/10.1016/j.apcatb.2012.11.017
981 [63] T.Aubert, F.Cabello-Hurtado, M. A. Esnault, C. Neaime, D. Lebret-Chauvel, S.
982 Jeanne, P. Pellen, C. Roiland, L. L. Polles, N. Saito, K. Kimoto, H. Haneda, N. Ohashi,
983 F. Grasset, Extended Investigations on Luminescent $Cs_2[Mo_6Br_{14}]@SiO_2$ Nanoparticles:
984 Physico-Structural Characterizations and Toxicity Studies. J. Phys. Chem. C, 17 (2013)
985 20154−20163. https://doi.org/10.1021/jp405836q
986 [64] M. N. Ivanova, Y. A. Vorotnikov, E. E. Plotnikova, M. V. Marchuk, A.A. Ivanov,
987 A. A. Ivanov, I. P. Asanov, A. R. Tsygankova, E. D. Grayfer, V. E. Fedorov, M. A.
988 Shestopalov, Hexamolybdenum Clusters Supported on Exfoliated h BN Nanosheets for
989 Photocatalytic Water Purification. Inorg. Chem., 9 (2020) 6439-6448.
990 https://doi.org/10.1021/acs.inorgchem.0c00528

991

992